CrystEngComm

PAPER

Cite this: *CrystEngComm*, 2017, **19**, 834

Syntheses, structural characterization and photophysical properties of two series of rare-earth-isonicotinic-acid containing Waugh-type manganomolybdates†

Peijun Gong, Yanyan Li, Cuiping Zhai, Jie Luo, Xuemeng Tian, Lijuan Chen* and Junwei Zhao*

Two classes of rare-earth-organic-containing Waugh-type manganomolybdates $(NH_4)_8\{[RE(Hina)(ina)(H_2O)_2][Mn^{IV}Mo_9O_{32}]\}_2{\cdot}12H_2O$ [RE = La^{3+} (**1**), Pr^{3+} (**2**), Nd^{3+} (**3**)] and $(NH_4)_3[RE(Hina)_2(H_2O)_6][Mn^{IV}Mo_9O_{32}]{\cdot}7H_2O$ [RE = Sm^{3+} (**4**), Eu^{3+} (**5**), Gd^{3+} (**6**), Tb^{3+} (**7**), Dy^{3+} (**8**), Ho^{3+} (**9**), Er^{3+} (**10**), Tm^{3+} (**11**), Yb^{3+} (**12**), Y^{3+} (**13**)] (Hina = isonicotinic acid) were prepared by means of a step-by-step synthetic strategy and further characterized by IR spectroscopy, elemental analyses, UV-visible spectroscopy and single-crystal X-ray diffraction. X-ray diffraction indicates that **1–3** consist of an organic–inorganic hybrid dimeric $\{[RE(Hina)(ina)(H_2O)_2][Mn^{IV}Mo_9O_{32}]\}_2^{8-}$ core constituted by two $[MnMo_9O_{32}]^{6-}$ units linked *via* a dinuclear $\{[RE(Hina)(ina)(H_2O)_2]_2\}^{4+}$ cation whereas **4–13** are composed of an organic–inorganic hybrid $[RE(Hina)_2(H_2O)_6]^{3+}$ fragment and one $[MnMo_9O_{32}]^{6-}$ polyoxoanion. It should be pointed out that the nature of RE cations controls these two structure types. As far as we know, **1–13** represent the first examples of Waugh-type manganomolybdates including rare-earth-organic subunits so far. Furthermore, their photocatalytic activities for the degradation of azophloxine were probed in aqueous medium and **3** and **8** as representatives were systematically investigated involving the influence of the optimal pH, catalyst dosage and the doping amount of VK-TA18 nanometer titanium dioxide on the photocatalytic activities. The solid-state photoluminescence properties and lifetime decay behaviors of **3**, **4** and **5** in UV-visible or near-infrared regions were also examined at ambient temperature.

Received 22nd November 2016,
Accepted 20th December 2016

DOI: 10.1039/c6ce02428a

www.rsc.org/crystengcomm

Introduction

The design and synthesis of polyoxometalate (POM)-based hybrid materials have received persistent attention not only because of their intriguing variety of architectures and fascinating topologies but also for their remarkable properties and potential applications in catalysis, medicine, nanotechnology and magnetic materials.[1] Over the past several decades, numerous POM-based hybrid materials structurally modified by various organic ligands,[2] transition metal (TM) ions[3] or TM–organic segments[3b,c,4] have been extensively prepared; however, exploration of these POM-based hybrid materials with rare earth (RE) ions or RE-organic subunits remains less developed, one reason for which may be that the highly oxophilic RE ions can be readily combined with POMs so that they often form amorphous precipitates instead of crystalline phases, which impede the structural determination of desired products.[5] There is no doubt that RE-containing POM-based materials (REPOMMs) exhibit not only aesthetic topological structures but also attractive functionalities such as magnetic, luminescence and catalytic properties.[6,7] Therefore, searching for and discovering novel REPOMMs have always been an extremely challenging and significant research topic with the profound development of POM chemistry. Furthermore, RE ions have flexible coordination geometries and variable coordination numbers in contrast to TM ions, which provide great possibilities in the pursuit of multifunctional REPOMMs.

The door of REPOMM chemistry was first opened by the groundbreaking work on $[REW_{10}O_{35}]^{7-}$ that was obtained by Peacock and Weakley in 1971.[8] Subsequently, REPOMMs, as a remarkable subclass of POMs, have attracted considerable concern due to their alluring structures as well as excellent physicochemical properties. Hitherto, a large number of REPOMMs have been prepared and crystallographically

Henan Key Laboratory of Polyoxometalate Chemistry, Institute of Molecular and Crystal Engineering, College of Chemistry and Chemical Engineering, Henan University, Kaifeng, Henan 475004, P. R. China. E-mail: ljchen@henu.edu.cn, zhaojunwei@henu.edu.cn

† Electronic supplementary information (ESI) available: Discussion on IR spectra, related structural figures, related UV and visible spectra, related photocatalytic figures and BVS parameters of **1**. CCDC 1515497–1515509. For ESI and crystallographic data in CIF or other electronic format see DOI: 10.1039/c6ce02428a

characterized. However, the majority of reported REPOMMs are RE-containing polyoxotungstates such as RE-silicotungstates,[8,9] RE-phosphotungstates,[10] RE-arsenotungstates,[11] RE-germanotungstates,[12] RE-iso-polyoxotungstates,[13] and so on.[14] Very recently, several types of RE-polyoxotungstate hybrid materials have also been isolated by our group.[15] In contrast, synthesis and exploration of RE-containing polyoxomolybdate (POMB) materials (REPOMBMs) are only in their infancy, principally because POMBs are not particularly stable in aqueous solution compared to polyoxotungstates.[16] Even so, in the past decade, some REPOMBMs were still discovered successively (some typical examples are demonstrated in the ESI†).[17–21] Obviously, the current interest on REPOMBMs is mainly concentrated on Anderson- or Keggin-type species; however, much less interest is involved in the field of Waugh-type REPOMBMs although the first Waugh-type POM was excavated by Struve in 1854.[22] To date, only two crystallographically characterized Waugh-type REPOMBMs are known, one of which is $[La_2(H_2O)_{12}(MnMo_9O_{32})]\cdot 2H_2O$ and the other is $[(CH_3)_4N]_2Nd[HMnMo_9O_{32}]\cdot 6H_2O$.[23] To the best of our knowledge, almost no RE-organic-containing Waugh-type POMB materials (REOCWPOMBMs) have been reported. Apparently, it remains a great and longstanding challenge to design and synthesize novel REOCWPOMBMs. Nevertheless, it is well known that the Waugh-type $[MnMo_9O_{32}]^{6-}$ polyoxoanion exhibits multiple coordination active sites and high surface negative charges, which can provide great possibilities for the construction of novel REOCWPOMBMs with neoteric structures and value-added properties.

Under this research background, searching for and discovering novel REOCWPOMBMs have gradually developed as a hot area of research with the persistent development of POM chemistry. As a part of our continuous work in discovering novel organic–inorganic hybrid POMB-based materials with the strategy of utilizing the reactions of $(NH_4)_6Mo_7O_{24}\cdot 4H_2O$ with TM and/or RE ions in the participation of functional organic ligands,[16] recently, we have paid attention to exploring novel REOCWPOMBMs by a step-by-step synthetic strategy. First, the self-assembly reaction between $(NH_4)_6(Mo_7O_{24})\cdot 4H_2O$ and $Mn(CH_3COO)_2\cdot 4H_2O$ and 30% H_2O_2 in a pH 5 environment in a 90 °C water bath was utilized to *in situ* form the aqueous solution containing the Waugh-type $[MnMo_9O_{32}]^{6-}$ polyoxoanion, and then a mixed water/DMF (*N*,*N*-dimethylformamide) solution containing RE^{3+} ions and isonicotinic acid (Hina) was added. Finally, slow evaporation of the filtrate led to the formation of the desired REOCWPOMBMs (Fig. 1). Thus, two types of unusual RE-isonicotinic-ligand-containing Waugh-type manganomolybdates $(NH_4)_8\{[RE(Hina)(ina)(H_2O)_2][Mn^{IV}Mo_9O_{32}]\}_2\cdot 12H_2O$ [RE = La^{3+} (**1**), Pr^{3+} (**2**), Nd^{3+} (**3**)] and $(NH_4)_3[RE(Hina)_2(H_2O)_6][Mn^{IV}Mo_9O_{32}]\cdot 7H_2O$ [RE = Sm^{3+} (**4**), Eu^{3+} (**5**), Gd^{3+} (**6**), Tb^{3+} (**7**), Dy^{3+} (**8**), Ho^{3+} (**9**), Er^{3+} (**10**), Tm^{3+} (**11**), Yb^{3+} (**12**), Y^{3+} (**13**)] were successfully synthesized *via* the conventional aqueous solution method. It should be noted that the nature of RE cations controls these two

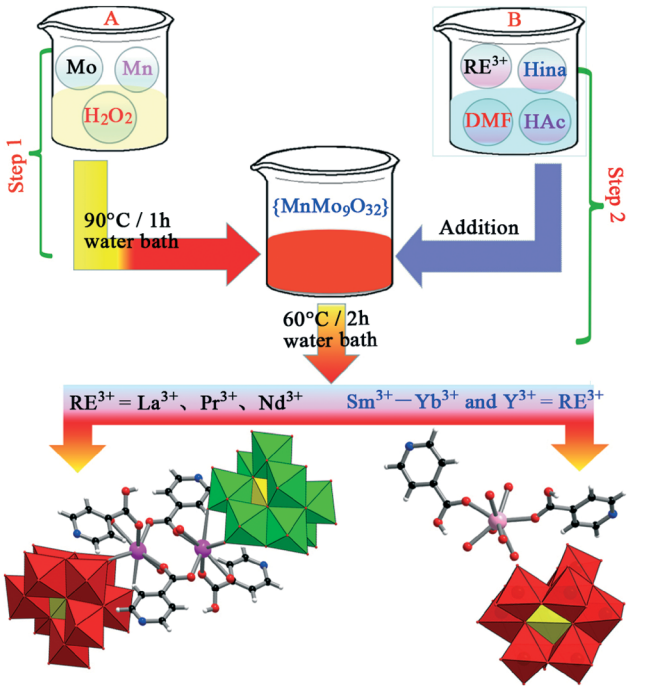

Fig. 1 Schematic synthetic process of **1–13** by a step-by-step synthetic strategy.

structure types. **1–3** exhibit a dimeric structure constructed from two Waugh-type $[MnMo_9O_{32}]^{6-}$ polyoxoanions connected by a double-ina-bridging di-RE $[RE(Hina)(ina)(H_2O)_2]^{4+}$ cluster through six terminal oxygen atoms, whereas **4–13** display a monomeric fashion defined by a Waugh-type $[MnMo_9O_{32}]^{6-}$ polyoxoanion and a discrete $[RE(Hina)_2(H_2O)_6]^{3+}$ cation. To the best of our knowledge, **1–13** represent the first examples of REOCWPOMBMs with Hina ligands to date. Furthermore, their photocatalytic activities for the degradation of azophloxine were systematically investigated and only **3** and **8** as representatives are discussed in detail. The solid-state photoluminescence properties and lifetime decay behaviors of **3–5** have been measured at room temperature and discussed in detail.

Experimental

Materials and physical measurements

All the chemical reagents were commercially available and used without further purification. IR spectra were recorded on a Nicolet 170 SXFT-IR spectrometer using KBr pellets in the range of 4000–400 cm^{-1}. UV-vis spectra and diffuse reflectance spectra were determined on a HITACHI U-4100 UV-vis-NIR spectrometer. C, H and N elemental analyses were performed on a Perkin-Elmer 2400-II CHNS/O analyzer. Photoluminescence spectra and decay lifetimes were investigated on an FLS 980 Edinburgh analytical instrument equipped with a 450 W xenon lamp and a μF900H high energy microsecond flashlamp as the excitation sources. The photocatalytic experiments were performed in an XPA photoreactor (Xujiang Electromechanical Plant, Nanjing, China)

equipped with a 300 W mercury lamp or a 500 W xenon lamp as the light source. First, the photocatalyst was added to a 50 mL solution containing azophloxine in a quartz glass tube. Afterwards, the mixed solution was then exposed to light irradiation under continuous magnetic stirring. At given time intervals, 3.0 mL of the azophloxine solution was taken out from the quartz glass tube, centrifuged and then filtered. The solution was analyzed using UV-vis spectroscopy.

Preparation of 1–13

$(NH_4)_8\{[La(Hina)(ina)(H_2O)_2][Mn^{IV}Mo_9O_{32}]\}_2\cdot 12H_2O$ (1). Solution A: $(NH_4)_6(Mo_7O_{24})\cdot 4H_2O$ (2.002 g, 1.620 mmol) was dissolved in 20 mL distilled water under stirring and then the pH value was adjusted to 5.0 with glacial acetic acid. After the solution was stirred for about 15 min, $Mn(CH_3COO)_2\cdot 4H_2O$ (0.120 g, 0.490 mmol) and 0.45 mL of 30% H_2O_2 solution were successively added. The mixture was stirred for *ca.* 15 min, kept in a 90 °C water bath for 1 h and filtered quickly. Orange-red microcrystals appeared as soon as the filtrate was cooled, and then 15 mL distilled water was added. The filtrate was heated and stirred for 5–10 min until the microcrystals were dissolved. Subsequently, solution B (solution B was formed by mixing $La(NO_3)_3\cdot 6H_2O$ (0.250 g, 0.577 mmol), Hina (0.269 g, 2.185 mmol), 10 mL distilled water, 2 mL glacial acetic acid, and 5 mL DMF (*N*,*N*-dimethylformamide) under stirring for 30 min at room temperature) was added into solution A. The resulting mixture was stirred for *ca.* 20 min, kept in a 60 °C water bath for 2 h and filtered. The filtrate was allowed to evaporate in air at room temperature. After about 2 days, orange block crystals of **1** suitable for X-ray diffraction were obtained. Yield: *ca.* 22% (based on $Mn(CH_3COO)_2\cdot 4H_2O$). Anal. calcd. (found, %) for $C_{24}H_{82}La_2Mn_2Mo_{18}N_{12}O_{88}$ (**1**): C 7.10 (6.88), H 2.03 (1.88), N 4.14 (3.97), Mn 2.70 (2.60), La 6.84 (6.97), Mo 42.52 (42.16). IR (KBr, cm^{-1}): 3425 (m), 3153 (m), 1589 (s), 1402 (s), 1247 (w), 1193 (w), 939 (s), 902 (s), 768 (m), 680 (s), 595 (s), 542 (s), 496 (s) (Fig. S1, ESI†).

$(NH_4)_8\{[Pr(Hina)(ina)(H_2O)_2][Mn^{IV}Mo_9O_{32}]\}_2\cdot 12H_2O$ (2). The preparation process of **2** was similar to that of **1** except that the same amount of $Pr(NO_3)_3\cdot 6H_2O$ was used instead of $La(NO_3)_3\cdot 6H_2O$. Orange block crystals of **2** were harvested after 2 days. Yield: *ca.* 25% (based on $Mn(CH_3COO)_2\cdot 4H_2O$). Anal. calcd. (found, %) for $C_{24}H_{82}Pr_2Mn_2\ Mo_{18}N_{12}O_{88}$ (**2**): C 7.10 (6.86), H 2.03 (1.90), N 4.13 (3.97), Mn 2.70 (2.59), Pr 6.93 (7.17), Mo 42.48 (42.15). IR (KBr, cm^{-1}): 3425 (m), 3153 (m), 1593 (s), 1402 (s), 1247 (w), 1193 (w), 935 (s), 900 (s), 768 (m), 681 (s), 594 (s), 542 (s), 495 (s) (Fig. S1, ESI†).

$(NH_4)_8\{[Nd(Hina)(ina)(H_2O)_2][Mn^{IV}Mo_9O_{32}]\}_2\cdot 12H_2O$ (3). The synthetic method of **3** was identical to that of **1** except for using the same amount of $Nd(NO_3)_3\cdot 6H_2O$ instead of $La(NO_3)_3\cdot 6H_2O$. Orange block crystals of **3** were isolated after 2 days. Yield: *ca.* 29% (based on $Mn(CH_3COO)_2\cdot 4H_2O$). Anal. calcd. (found, %) for $C_{24}H_{82}Nd_2\ Mn_2Mo_{18}N_{12}O_{88}$ (**3**): C 7.08 (6.82), H 2.03 (1.87), N 4.13 (3.96), Mn 2.70 (2.56), Nd 7.08 (7.22), Mo 42.41 (42.14). IR (KBr, cm^{-1}): 3425 (m), 3155 (m), 1591 (s), 1403 (s), 1248 (w), 1193 (w), 941 (s), 901 (s), 769 (m), 680 (s), 595 (s), 541 (s), 494 (s) (Fig. S1, ESI†).

$(NH_4)_3[Sm(Hina)_2(H_2O)_6][Mn^{IV}Mo_9O_{32}]\cdot 7H_2O$ (4). The synthetic method of **4** was similar to the preparation of **1** except that solution B contains $Sm(NO_3)_3\cdot 6H_2O$ (0.345 g, 0.776 mmol), Hina (0.156 g, 1.267 mmol), 10 mL distilled water, 2 mL glacial acetic acid and 1 mL DMF. Orange needle-like crystals of **4** suitable for X-ray diffraction were obtained after about 1 day. Yield: *ca.* 33% (based on $Mn(CH_3COO)_2\cdot 4H_2O$). Anal. calcd. (found, %) for $C_{12}H_{48}SmMnMo_9N_5O_{49}$ (**4**): C 6.81 (6.95), H 2.29 (2.14), N 3.31 (3.17), Mn 2.60 (2.48), Sm 7.11 (7.25), Mo 40.82 (40.50). IR (KBr, cm^{-1}): 3400 (m), 3167 (m), 1598 (s), 1510 (w), 1403 (s), 1248 (m), 1197 (w), 1000 (w), 939 (s), 902 (s), 770 (m), 678 (s), 595 (s), 542 (s), 494 (s) (Fig. S1, ESI†).

$(NH_4)_3[Eu(Hina)_2(H_2O)_6][Mn^{IV}Mo_9O_{32}]\cdot 7H_2O$ (5). The synthetic method of **5** was identical to the preparation of **4** except for using a different amount of $Eu(NO_3)_3\cdot 6H_2O$ (0.499 g, 1.119 mmol) in place of $Sm(NO_3)_3\cdot 6H_2O$ (0.345 g, 0.776 mmol). Orange needle-like crystals of **5** were obtained. Yield: *ca.* 50% (based on $Mn(CH_3COO)_2\cdot 4H_2O$). Anal. calcd. (found, %) for $C_{12}H_{48}EuMnMo_9N_5O_{49}$ (**5**): C 6.81 (6.93), H 2.28 (2.10), N 3.31 (3.23), Mn 2.60 (2.49), Eu 7.18 (7.29), Mo 40.79 (40.43). IR (KBr, cm^{-1}): 3400 (m), 3170 (m), 1594 (s), 1500 (w), 1403 (s), 1248 (m), 1200 (w), 1008 (w), 935 (s), 905 (s), 769 (m), 680 (s), 595 (s), 540 (s), 493 (s) (Fig. S1, ESI†).

$(NH_4)_3[Gd(Hina)_2(H_2O)_6][Mn^{IV}Mo_9O_{32}]\cdot 7H_2O$ (6). The synthetic procedure was identical to that of **5**, but we used the same amount of $Gd(NO_3)_3\cdot 6H_2O$ instead of $Eu(NO_3)_3\cdot 6H_2O$. Orange needle-like crystals of **6** were obtained. Yield: *ca.* 61% (based on $Mn(CH_3COO)_2\cdot 4H_2O$). Anal. calcd. (found, %) for $C_{12}H_{48}GdMnMo_9N_5O_{49}$ (**6**): C 6.80 (6.95), H 2.28 (2.14), N 3.30 (3.21), Mn 2.59 (2.48), Gd 7.41 (7.55), Mo 40.69 (40.38). IR (KBr, cm^{-1}): 3400 (m), 3172 (m), 1594 (s), 1500 (w), 1403 (s), 1248 (m), 1200 (w), 1008 (w), 935 (s), 905 (s), 769 (m), 682 (s), 595 (s), 541 (s), 493 (s) (Fig. S1, ESI†).

$(NH_4)_3[Tb(Hina)_2(H_2O)_6][Mn^{IV}Mo_9O_{32}]\cdot 7H_2O$ (7). The synthetic procedure was identical to that of **5**, but we used the same amount of $Tb(NO_3)_3\cdot 6H_2O$ instead of $Eu(NO_3)_3\cdot 6H_2O$. Orange needle-like crystals of **7** were collected. Yield: *ca.* 68% (based on $Mn(CH_3COO)_2\cdot 4H_2O$). Anal. calcd. (found, %) for $C_{12}H_{48}TbMnMo_9N_5O_{49}$ (**7**): C 6.79 (6.90), H 2.28 (2.12), N 3.30 (3.19), Mn 2.59 (2.41), Tb 7.48 (7.66), Mo 40.66 (40.29). IR (KBr, cm^{-1}): 3400 (m), 3170 (m), 1596 (s), 1500 (w), 1401 (s), 1248 (m), 1201 (w), 1008 (w), 936 (s), 905 (s), 769 (m), 683 (s), 595 (s), 541 (s), 493 (s) (Fig. S1, ESI†).

$(NH_4)_3[Dy(Hina)_2(H_2O)_6][Mn^{IV}Mo_9O_{32}]\cdot 7H_2O$ (8). The synthetic procedure was identical to that of **5**, but we used the same amount of $Dy(NO_3)_3\cdot 6H_2O$ instead of $Eu(NO_3)_3\cdot 6H_2O$. Orange needle-like crystals were collected. Yield: *ca.* 72% (based on $Mn(CH_3COO)_2\cdot 4H_2O$). Anal. calcd. (found, %) for $C_{12}H_{48}DyMnMo_9N_5O_{49}$ (**8**): C 6.77 (6.86), H 2.27 (2.16), N 3.29 (3.15), Mn 2.58 (2.38), Dy 7.64 (7.78), Mo 40.59 (40.31). IR (KBr, cm^{-1}): 3400 (m), 3170 (m), 1599 (s), 1500 (w), 1402 (s), 1248 (m), 1201 (w), 1008 (w), 936 (s), 905 (s), 769 (m), 684 (s), 595 (s), 541 (s), 493 (s) (Fig. S1, ESI†).

$(NH_4)_3[Ho(Hina)_2(H_2O)_6][Mn^{IV}Mo_9O_{32}]\cdot 7H_2O$ (9). The synthetic procedure was identical to that of **5**, but we used the same amount of $Ho(NO_3)_3\cdot 6H_2O$ instead of $Eu(NO_3)_3\cdot 6H_2O$. Orange needle-like crystals were collected. Yield: *ca.* 71% (based on $Mn(CH_3COO)_2\cdot 4H_2O$). Anal. calcd. (found, %) for $C_{12}H_{48}HoMnMo_9N_5O_{49}$ (**9**): C 6.77 (6.89), H 2.27 (2.12), N 3.29 (3.20), Mn 2.58 (2.39), Ho 7.74 (7.91), Mo 40.54 (40.23). IR (KBr, cm^{-1}): 3400 (m), 3170 (m), 1599 (s), 1500 (w), 1400 (s), 1248 (m), 1200 (w), 1008 (w), 935 (s), 905 (s), 769 (m), 684 (s), 594 (s), 541 (s), 493 (s) (Fig. S1, ESI†).

$(NH_4)_3[Er(Hina)_2(H_2O)_6][Mn^{IV}Mo_9O_{32}]\cdot 7H_2O$ (10). The synthetic procedure was identical to that of **5**, but we used the same amount of $Er(NO_3)_3\cdot 6H_2O$ instead of $Eu(NO_3)_3\cdot 6H_2O$. Orange needle-like crystals were collected. Yield: *ca.*72% (based on $Mn(CH_3COO)_2\cdot 4H_2O$). Anal. calcd. (found, %) for $C_{12}H_{48}ErMnMo_9N_5O_{49}$ (**10**): C 6.76 (6.89), H 2.27 (2.15), N 3.28 (3.19), Mn 2.58 (2.41), Er 7.84 (7.93), Mo 40.50 (40.24). IR (KBr, cm^{-1}): 3400 (m), 3170 (m), 1603 (s), 1500 (w), 1396 (s), 1248 (m), 1200 (w), 1008 (w), 935 (s), 905 (s), 769 (m), 685 (s), 594 (s), 541 (s), 493 (s) (Fig. S1, ESI†).

$(NH_4)_3[Tm(Hina)_2(H_2O)_6][Mn^{IV}Mo_9O_{32}]\cdot 7H_2O$ (11). The synthetic procedure was identical to that of **5**, but we used the same amount of $Tm(NO_3)_3\cdot 6H_2O$ instead of $Eu(NO_3)_3\cdot 6H_2O$. Orange needle-like crystals were collected. Yield: *ca.* 70% (based on $Mn(CH_3COO)_2\cdot 4H_2O$). Anal. calcd. (found, %) for $C_{12}H_{48}TmMnMo_9N_5O_{49}$ (**11**): C 6.75 (6.90), H 2.27 (2.11), N 3.28 (3.17), Mn 2.57 (2.39), Tm 7.92 (8.06), Mo 40.47 (40.12). IR (KBr, cm^{-1}): 3400 (m), 3170 (m), 1603 (s), 1500 (w), 1399 (s), 1248 (m), 1200 (w), 1008 (w), 935 (s), 905 (s), 769 (m), 683 (s), 594 (s), 541 (s), 493 (s) (Fig. S1, ESI†).

$(NH_4)_3[Yb(Hina)_2(H_2O)_6][Mn^{IV}Mo_9O_{32}]\cdot 7H_2O$ (12). The synthetic procedure was identical to that of **5**, but we used the same amount of $Yb(NO_3)_3\cdot 6H_2O$ instead of $Eu(NO_3)_3\cdot 6H_2O$. Orange needle-like crystals were collected. Yield: *ca.* 73% (based on $Mn(CH_3COO)_2\cdot 4H_2O$). Anal. calcd. (found, %) for $C_{12}H_{48}YbMnMo_9N_5O_{49}$ (**12**): C 6.74 (6.87), H 2.26 (2.15), N 3.28 (3.10), Mn 2.57 (2.41), Yb 8.09 (8.22), Mo 40.39 (39.97). IR (KBr, cm^{-1}): 3400 (m), 3170 (m), 1607 (s), 1500 (w), 1399 (s), 1248 (m), 1200 (w), 1008 (w), 935 (s), 905 (s), 769 (m), 680 (s), 594 (s), 541 (s), 493 (s) (Fig. S1, ESI†).

$(NH_4)_3[Y(Hina)_2(H_2O)_6][Mn^{IV}Mo_9O_{32}]\cdot 7H_2O$ (13). The synthetic procedure was identical to that of **5**, but we used the same amount of $Y(NO_3)_3\cdot 6H_2O$ instead of $Eu(NO_3)_3\cdot 6H_2O$. Orange needle-like crystals were collected. Yield: *ca.* 68% (based on $Mn(CH_3COO)_2\cdot 4H_2O$). Anal. calcd. (found, %) for $C_{12}H_{48}YMnMo_9N_5O_{49}$ (**13**): C 7.02 (7.16), H 2.36 (2.28), N 3.41 (3.53), Mn 2.67 (2.53), Y 4.33 (4.41), Mo 42.04 (41.86). IR (KBr, cm^{-1}): 3400 (m), 3170 (m), 1603 (s), 1500 (w), 1399 (s), 1248 (m), 1200 (w), 1008 (w), 935 (s), 905 (s), 769 (m), 685 (s), 594 (s), 541 (s), 493 (s) (Fig. S1, ESI†).

X-ray crystallography

A suitable good-quality single crystal of **1–13** was mounted on a glass capillary. Their diffraction intensity data were collected at 296(2) K on a Bruker APEX II CCD detector (Mo Kα radiation λ = 0.71073 Å). Routine Lorentz and polarization corrections and an empirical absorption correction were applied. Direct methods were used to solve their structures and locate the heavy atoms using the SHELXTL-97 program package.[24] The remaining atoms were found from successive full-matrix least-squares refinements on F^2 and Fourier syntheses. The non-hydrogen atoms were refined anisotropically and the hydrogen atoms linking to carbon and nitrogen atoms were geometrically placed. All the hydrogen atoms were isotropically refined in a riding mode using the default SHELXL parameters. No hydrogen atoms associated with water molecules and ammonium ions were located from the difference Fourier map. This phenomenon is very common in POM chemistry.[11–13] The crystallographic and structural refinement parameters of **1–13** are illustrated in Table 1. Crystallographic data in this paper have been deposited in the Cambridge Crystallographic Data Centre with CCDC 1515497–1515509 for **1–13**, respectively.

Results and discussion

Synthesis

Our interest in preparing novel REOCPOMMs is derived not only from the fact that the POMs' own remarkable rich redox properties owing to the variability of their molecular properties including size, shape and charge density[1d,25a–c] and the ability of POMs to accommodate multiple electrons inside their frameworks can make them intriguing multi-electron transfer catalysts,[25c–g] but also that highly oxyphilic RE ions with multiple coordination requirements can provide a large possibility for assembling REPOMMs with fascinating structures and interesting properties.[25h–j] To date, relevant reports on REOCWPOMMs are very limited, which provides us an excellent opportunity to probe this domain. Therefore, we selected the system containing the $[MnMo_9O_{32}]^{6-}$ polyoxoanion, RE^{3+} cations and Hina ligands to exploit neoteric REOCWPOMMs. Herein, a step-by-step synthetic strategy was utilized. The reaction of $(NH_4)_6(Mo_7O_{24})\cdot 4H_2O$, $Mn(CH_3COO)_2\cdot 4H_2O$ and 30% H_2O_2 led to *in situ* formation of the Waugh-type $[MnMo_9O_{32}]^{6-}$ polyanion, and then a mixed solution containing RE^{3+} ions and Hina was introduced to prepare the anticipated REOCWPOMBMs. By this synthetic strategy, thirteen RE-isonicotinic-acid containing Waugh-type manganomolybdates were obtained under similar conditions. Experimental results indicate that the nature of RE^{3+} cations of the reaction system plays a significant role in influencing the structures of these compounds. During the course of our exploration, when La^{3+}, Pr^{3+} and Nd^{3+} cations were first employed, the dimeric hybrid species **1–3** were isolated, which are constructed from two Waugh-type $[MnMo_9O_{32}]^{6-}$ polyanions connected by a double-ina-bridging di-RE^{3+} $[RE(Hina)(ina)(H_2O)_2]^{4+}$ cluster. When other RE^{3+} cations (Sm^{3+}–Yb^{3+} and Y^{3+}) were used under similar conditions, the monomeric Waugh-type manganomolybdates **4–13** were

Table 1 X-ray diffraction crystallographic data and structure refinements for **1–13**

	1	2	3	4	5	6
Empirical formula	$C_{24}H_{82}La_2Mn_2Mo_{18}N_{12}O_{88}$	$C_{24}H_{82}Pr_2Mn_2Mo_{18}N_{12}O_{88}$	$C_{24}H_{82}Nd_2Mn_2Mo_{18}N_{12}O_{88}$	$C_{12}H_{48}SmMnMo_9N_5O_{49}$	$C_{12}H_{48}EuMnMo_9N_5O_{49}$	$C_{12}H_{48}GdMnMo_9N_5O_{49}$
Formula weight	4061.64	4065.64	4072.30	2115.30	2116.91	2122.20
Crystal system	Triclinic	Triclinic	Triclinic	Orthorhombic	Orthorhombic	Orthorhombic
Space group	$P\bar{1}$	$P\bar{1}$	$P\bar{1}$	*Pbca*	*Pbca*	*Pbca*
a, Å	10.3698(6)	10.4310(5)	10.4141(4)	19.0792(9)	19.0464(6)	19.0411(9)
b, Å	12.6471(8)	12.6785(6)	12.6941(5)	22.8325(10)	22.8077(7)	22.8346(11)
c, Å	19.0794(11)	19.1442(9)	19.1513(9)	24.3310(11)	24.2799(7)	24.2724(11)
α, deg	73.3200(10)	72.9560(10)	72.8930(10)	90	90	90
β, deg	81.7980(10)	82.0200(10)	82.0370(10)	90	90	90
γ, deg	88.7750(10)	89.2550(10)	89.3050(10)	90	90	90
V, Å^{-3}	2371.9(2)	2396.1(2)	2395.32(17)	10 599.2(8)	10 547.3(6)	10 553.5(9)
Z	1	1	1	8	8	8
μ, mm^{-1}	3.553	3.642	3.710	3.493	3.586	3.652
F(000)	1934	1938	1940	8096	8104	8112
T, K	296(2)	296(2)	296(2)	296(2)	296(2)	296(2)
Limiting indices	$-12 \le h \le 11$ $-15 \le k \le 14$ $-21 \le l \le 22$	$-10 \le h \le 12$ $-15 \le k \le 14$ $-22 \le l \le 19$	$-12 \le h \le 10$ $-15 \le k \le 15$ $-22 \le l \le 19$	$-22 \le h \le 22$ $-19 \le k \le 27$ $-28 \le l \le 28$	$-22 \le h \le 22$ $-27 \le k \le 25$ $-28 \le l \le 22$	$-22 \le h \le 22$ $-25 \le k \le 27$ $-26 \le l \le 28$
No. of reflections collected	12 125	12 283	12 304	52 019	52 197	52 008
No. of independent reflections	8246	8336	8326	9280	9296	9252
R_{int}	0.0257	0.0203	0.0220	0.0348	0.0479	0.0650
Data/restrains/parameters	8246/0/636	8336/0/637	8326/0/637	9280/0/679	9296/0/679	9252/0/679
GOF on F^2	1.070	1.038	1.048	1.073	1.064	1.025
Final R indices [$I > 2\sigma(I)$]	R_1 = 0.0467 wR_2 = 0.1219	R_1 = 0.0326 wR_2 = 0.0820	R_1 = 0.0361 wR_2 = 0.0919	R_1 = 0.0271 wR_2 = 0.0709	R_1 = 0.0320 wR_2 = 0.0846	R_1 = 0.0347 wR_2 = 0.0805
R indices (all data)	R_1 = 0.0633 wR_2 = 0.1306	R_1 = 0.0420 wR_2 = 0.0861	R_1 = 0.0474 wR_2 = 0.0974	R_1 = 0.0349 wR_2 = 0.0745	R_1 = 0.0459 wR_2 = 0.0898	R_1 = 0.0551 wR_2 = 0.0870
Largest diff. peak and hole, e Å^{-3}	1.623, −2.602	1.705, −2.937	1.981, −3.130	2.109, −0.980	1.902, −0.878	2.006, −0.959

	7	8	9	10	11	12	13
Empirical formula	$C_{12}H_{48}TbMnMo_9N_5O_{49}$	$C_{12}H_{48}DyMnMo_9N_5O_{49}$	$C_{12}H_{48}HoMnMo_9N_5O_{49}$	$C_{12}H_{48}ErMnMo_9N_5O_{49}$	$C_{12}H_{48}TmMnM_9N_5O_{49}$	$C_{12}H_{48}YbMnMo_9N_5O_{49}$	$C_{12}H_{48}YMnMo_9N_5O_{49}$
Formula weight	2123.87	2127.45	2129.88	2132.21	2133.88	2137.99	2053.86
Crystal system	Orthorhombic	Orthorhombic	Orthorhombic	Orthorhombic	Orthorhombic	Orthorhombic	Orthorhombic
Space group	*Pbca*	*Pbca*	*Pbca*	*Pbca*	*Pbca*	*Pbca*	*Pbca*
a, Å	19.0677(16)	19.0233(6)	18.9918(8)	19.100(7)	18.9956(7)	18.9941(11)	18.9813(11)
b, Å	22.7335(19)	22.7722(7)	22.8191(10)	22.960(8)	22.8143(9)	22.8037(14)	22.8264(14)
c, Å	24.228(2)	24.1995(7)	24.1887(11)	24.338(9)	24.1926(10)	24.1386(14)	24.1927(14)
α, deg	90	90	90	90	90	90	90
β, deg	90	90	90	90	90	90	90
γ, deg	90	90	90	90	90	90	90
V, Å^{-3}	10 502.2(15)	10 483.3(6)	10 482.8(8)	10 673(6)	10 484.4(7)	10 455.3(11)	10 482.1(11)
Z	8	8	8	8	8	8	8
μ, mm^{-1}	3.754	3.837	3.921	3.941	4.104	4.207	3.524
F(000)	8120	8128	8136	8144	8152	8160	7912
T, K	296(2)	296(2)	296(2)	296(2)	296(2)	296(2)	296(2)
Limiting indices	$-22 \le h \le 22$	$-22 \le h \le 22$	$-22 \le h \le 22$	$-22 \le h \le 22$	$-22 \le h \le 22$	$-22 \le h \le 22$	$-22 \le h \le 22$

Table 1 *(continued)*

	7	8	9	10	11	12	13
	$-27 \le k \le 20$	$-26 \le k \le 26$	$-19 \le k \le 27$	$-27 \le k \le 21$	$-23 \le k \le 27$	$-27 \le k \le 27$	$-27 \le k \le 25$
	$-28 \le l \le 28$	$-21 \le l \le 28$	$-28 \le l \le 28$	$-28 \le l \le 28$	$-27 \le l \le 28$	$-21 \le l \le 28$	$-26 \le l \le 28$
No. of reflections collected	52 003	51 864	51 959	52 747	51 963	51 790	51 796
No. of independent reflections	9248	9236	9242	9389	9248	9205	9194
R_{int}	0.0371	0.0499	0.0783	0.0753	0.0374	0.0423	0.0614
Data/restrains/parameters	9248/0/679	9236/0/679	9242/6/679	9389/0/678	9248/0/679	9205/0/679	9194/0/678
GOF on F^2	1.086	1.072	1.077	1.051	1.041	1.064	1.052
Final R indices [$I > 2\sigma(I)$]	$R_1 = 0.0300$	$R_1 = 0.0348$	$R_1 = 0.0410$	$R_1 = 0.0391$	$R_1 = 0.0309$	$R_1 = 0.0321$	$R_1 = 0.0360$
	$wR_2 = 0.0808$	$wR_2 = 0.1025$	$wR_2 = 0.1055$	$wR_2 = 0.0943$	$wR_2 = 0.0865$	$wR_2 = 0.0887$	$wR_2 = 0.0888$
R indices (all data)	$R_1 = 0.0394$	$R_1 = 0.0506$	$R_1 = 0.0675$	$R_1 = 0.0640$	$R_1 = 0.0393$	$R_1 = 0.0423$	$R_1 = 0.0564$
	$wR_2 = 0.0853$	$wR_2 = 0.1147$	$wR_2 = 0.1228$	$wR_2 = 0.1020$	$wR_2 = 0.0901$	$wR_2 = 0.0928$	$wR_2 = 0.0950$
Largest diff. peak and hole, e Å^{-3}	2.339, −0.928	2.014, −1.022	2.138, −0.970	1.889, −0.875	2.177, −1.395	2.239, −0.852	1.993, −0.941

obtained, which are all composed of a Waugh-type $[MnMo_9O_{32}]^{6-}$ polyanion and a discrete $[RE(Hina)_2(H_2O)_6]^{3+}$ cation. It is supposed that this result may be related to lanthanide contraction. Similar phenomena were also observed in our preparations of REPOMMs.[26] For example, during the process of synthesizing the RE-containing isopolyoxotungstates in the presence of dimethylamine hydrochloride in acidic aqueous solution, the utilization of Pr^{3+}, Nd^{3+} and Sm^{3+} ions resulted in the 1-D chain-like architectures $[H_2N(CH_3)_2]_6Na_6[RE_4(H_2O)_{22}W_{28}O_{94}H_2]_2{\cdot}113H_2O$ formed by hexameric RE_8-comprising $[RE_4(H_2O)_{22}W_{28}O_{94}H_2]_2^{12-}$ entities *via* $[RE(H_2O)_5]^{3+}$ connectors; the introduction of the Eu^{3+} ion led to a 2-D sheet $Na_2[Eu(H_2O)_7]_2[Eu(H_2O)_5]_2[W_{22}O_{74}H_2]{\cdot}20H_2O$ constructed from 22-isopolytungstate $[W_{22}O_{74}H_2]^{14-}$ polyoxoanions and Eu^{3+} cations whereas other middle and late RE^{3+} ions can form the discrete structures $Na_3H_2[RE(H_2O)_4][RE(H_2O)_5]_2[W_{22}O_{74}H_2]{\cdot}36H_2O$ (RE = Gd^{3+}, Tb^{3+}, Er^{3+}, Tm^{3+}, Yb^{3+}, Lu^{3+}).[26a] In addition, the introduction of the Hina ligand also plays an important role in the construction of **1–13**. Firstly, as mentioned above, the highly oxophilic RE^{3+} ions can readily combine with POM precursors and form amorphous precipitates instead of crystallizing. It is known that organic ligands can effectively coordinate with RE^{3+} ions giving rise to RE-organic complexes, which can in some degree prevent the formation of precipitates derived from the direct combination of POM precursors and RE^{3+} ions.[5c,27] Herein, Hina was selected as the coordinate agent because it contains a carboxylic group that can coordinate or chelate RE^{3+} cations, which is favorable to the formation of REOCWPOMMs. Secondly, for solution A, if the hydrogen peroxide used is too much or too little, the $[MnMo_9O_{32}]^{6-}$ polyoxoanion would not form. Our experimental results show that the optimal usage of hydrogen peroxide (30%) is 0.45–0.9 mL in our reaction system. For solution B, the amount of $RE(NO_3)_3{\cdot}6H_2O$ is also a vital factor during the whole reaction period. The amount of $RE(NO_3)_3{\cdot}6H_2O$ is in the range of 0.20–0.27 g in the preparation of **1–3**. If the amount of $RE(NO_3)_3{\cdot}6H_2O$ exceeds 0.27 g, precipitates will be generated. When the amount of $RE(NO_3)_3{\cdot}6H_2O$ is lower than 0.20 g, the yields of products are too low or even no target product is afforded. **4–13** can be obtained within a wide range of amounts of $RE(NO_3)_3{\cdot}6H_2O$ varying from 0.30 g to 1.0 g except for $Sm(NO_3)_3{\cdot}6H_2O$ with an appropriate range of 0.37–0.50 g. Even if the amount of $RE(NO_3)_3{\cdot}6H_2O$ exceeds 1.0 g, the target products can still be isolated. Paralleling the experimental results reveals that the optimal usage of $Sm(NO_3)_3{\cdot}6H_2O$ is 0.35 g and the optimal usage of other $RE(NO_3)_3{\cdot}6H_2O$ is 0.50 g. Apparently, the continuous exploration of the REOCWPOMMs still remains a great challenge to us. Further work is in progress for exploiting novel Waugh-type POM-based materials and potential applications.

Structural description

Single-crystal X-ray diffraction reveals that the heteropolymolybdate $[MnMo_9O_{32}]^{6-}$ polyoxoanions in **1–13** are

identical and exhibit a typical Waugh-type structure. This Waugh-type $[MnMo_9O_{32}]^{6-}$ polyoxoanion (the atom numbering scheme in the polyoxoanion is from the crystallographic data of **1**) is constructed from a central MnO_6 octahedron and nine MoO_6 octahedra in an edge-sharing fashion (Fig. 2a). Interestingly, the structure of this polyoxoanion can also be understood as follows: a central MnO_6 octahedron is surrounded by three MoO_6 (Mo1, Mo5 and Mo9) octahedra arranged on three vertices of a triangle, giving rise to a Mn-centered triangular $\{MnMo_3O_{18}\}$ cluster (Fig. 2b and S2a in the ESI†) and then two edge-sharing Mo_3O_{13} triads (one Mo_3O_{13} triad is formed by Mo2, Mo3 and Mo4 and the other Mo_3O_{13} triad is constructed from Mo6, Mo7 and Mo8) are respectively capped above and below the Mn-centered triangular $\{MnMo_3O_{18}\}$ cluster (Fig. 2b). Specifically speaking, the Mo1, Mo5 and Mo9 atoms form an equilateral triangle (denoted as △2) with a Mo···Mo distance of *ca.* 5.5 Å and the Mn atom is located in the center of △2 with a Mn···Mo distance of *ca.* 3.2 Å. Moreover, the Mo2, Mo3, Mo4 atoms and the Mo6, Mo7, Mo8 atoms establish another two equilateral triangles △1 with a Mo···Mo distance of *ca.* 3.3 Å and △3 with a Mo···Mo distance of *ca.* 3.3 Å, respectively. It is noteworthy that the three equilateral triangles are parallel to each other and the distances of △2 to △1 and △3 are equal (Fig. 2c and S2b in the ESI†). Based on the above discussion, we can deduce that the polyoxoanion has an ideal D_3 point symmetry.[28] The C_3 axis passes through the centers of the three equilateral triangles and three C_2 axes pass though the three vertices and the central of the △2, respectively (Fig. 2c). Moreover, the Mo2, Mo3, Mo4 atoms and the Mo6, Mo7, Mo8 atoms are respectively combined with the Mn center through the bridging oxygen atoms, resulting in the corner-sharing double cubane-like $\{MnMo_6O_8\}$ structure (Fig. 2d). As we all know, cubane-type mixed-metal clusters are a unique and intriguing area in cluster chemistry due to their charming structures and potential applications in optics, catalysis, electrochemistry and materials science.[29] Hitherto, some Mo-containing heterometallic cubane-like clusters,[30,31] isometallic cubane $\{M_4O_4\}$ or heterometallic cubane $\{M'_xM_{4-x}O_4\}$ containing POMs,[32a–d] and multi-$\{M_4O_4\}$ cubane encapsulated POM oligomers[32e–h] have been reported (see the ESI†).

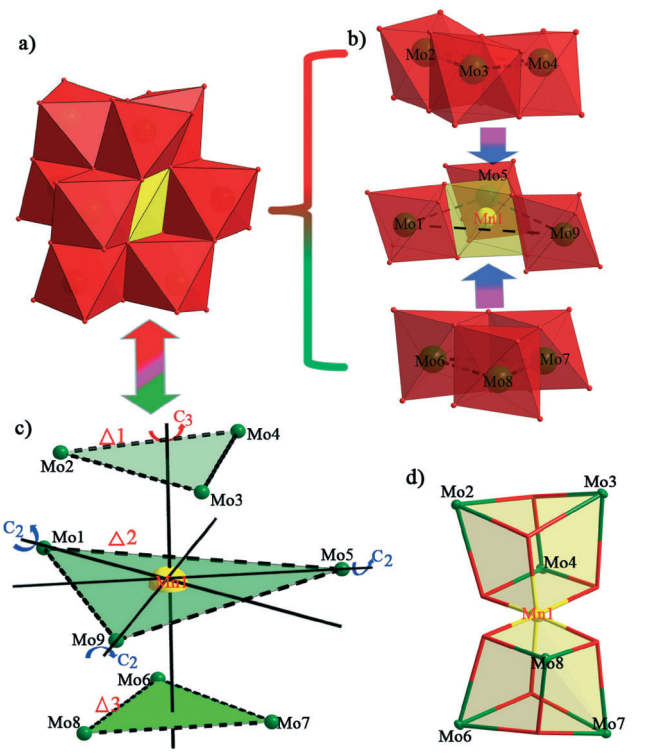

Fig. 2 (a) The structure of the $[MnMo_9O_{32}]^{6-}$ polyoxoanion in **1**. (b) The combination of the planar $\{MnMo_3O_{18}\}$ cluster and two groups of edge-sharing $\{Mo_3O_{13}\}$ triads. (c) Three triangles (△1, △2, △3) in the $[MnMo_9O_{32}]^{6-}$ polyoxoanion with the ideal D_3 point symmetry. (d) The corner-sharing double cubane-like $\{MnMo_6O_8\}$ structure in the $[MnMo_9O_{32}]^{6-}$ polyoxoanion.

Single-crystal X-ray diffraction analysis indicates that **1–3** are isomorphous and crystallize in the triclinic space group $P\bar{1}$ while **4–13** are isomorphic and crystallize in the orthorhombic space group *Pbca*. Therefore, only **1** and **10** are representatively described in detail herein. The molecular structure of **1** consists of one inorganic–organic hybrid dimeric $\{[La(Hina)(ina)(H_2O)_2][Mn^{IV}Mo_9O_{32}]\}_2^{8-}$ core (Fig. 3a), eight free NH_4^+ cations and twelve lattice water molecules. Bond valence sum (BVS) calculations[33] indicate that the oxidation states of Mo, Mn and La centers are +6, +4 and +3, respectively (Table S1, ESI†), which are well consistent with their coordination geometries. The centrosymmetric dimeric core is constituted by two asymmetrical $\{[La(Hina)(ina)(H_2O)_2][Mn^{IV}Mo_9O_{32}]\}^{4-}$ subunits bridged by two $(\eta,^2\mu\text{-}1,1)$-ina ligands. In the $\{[La(Hina)(ina)(H_2O)_2][Mn^{IV}Mo_9O_{32}]\}^{4-}$ subunit, the crystallographically independent $La1^{3+}$ ion exhibits a nine-coordinate distorted monocapped square antiprismatic geometry defined by three terminal oxygen atoms from the tridentate $[MnMo_9O_{32}]^{6-}$ polyoxoanion and two coordinate water oxygen atoms and four carboxyl oxygen atoms from a monodentate Hina ligand, a bidentate ina ligand and another Hina ligand on the other $\{[La(Hina)(ina)(H_2O)_2][Mn^{IV}Mo_9O_{32}]\}^{4-}$ subunit with La–O bond lengths of 2.491(8)–2.964(7) Å. In the monocapped square antiprismatic coordination geometry of the $La1^{3+}$ cation, the O19, O26, O35A and O1W group and the O34, O35, O36 and O2W group constitute the two bottom surfaces of the square antiprism and their standard deviations are 0.1256 and 0.0998 Å, respectively. The dihedral angle between the two bottom surfaces is 3.1°. The distances between the $La1^{3+}$ cation and the two bottom surfaces are 0.8150 and 1.6658 Å, respectively. The O23 atom occupies the cap position covering the bottom surface defined by the O19, O26, O35A and O1W group and the distance between the O23 atom and the bottom surface is 1.7017 Å (Fig. 3b). From the above-mentioned data, the coordination geometry of the $La1^{3+}$ cation is severely distorted, the main reason for which is related to the fact that the ina ligands have a large steric hindrance in the construction of the structure. Moreover, the long La1–O35 distance [2.964(7) Å] can further confirm the existence of the large steric

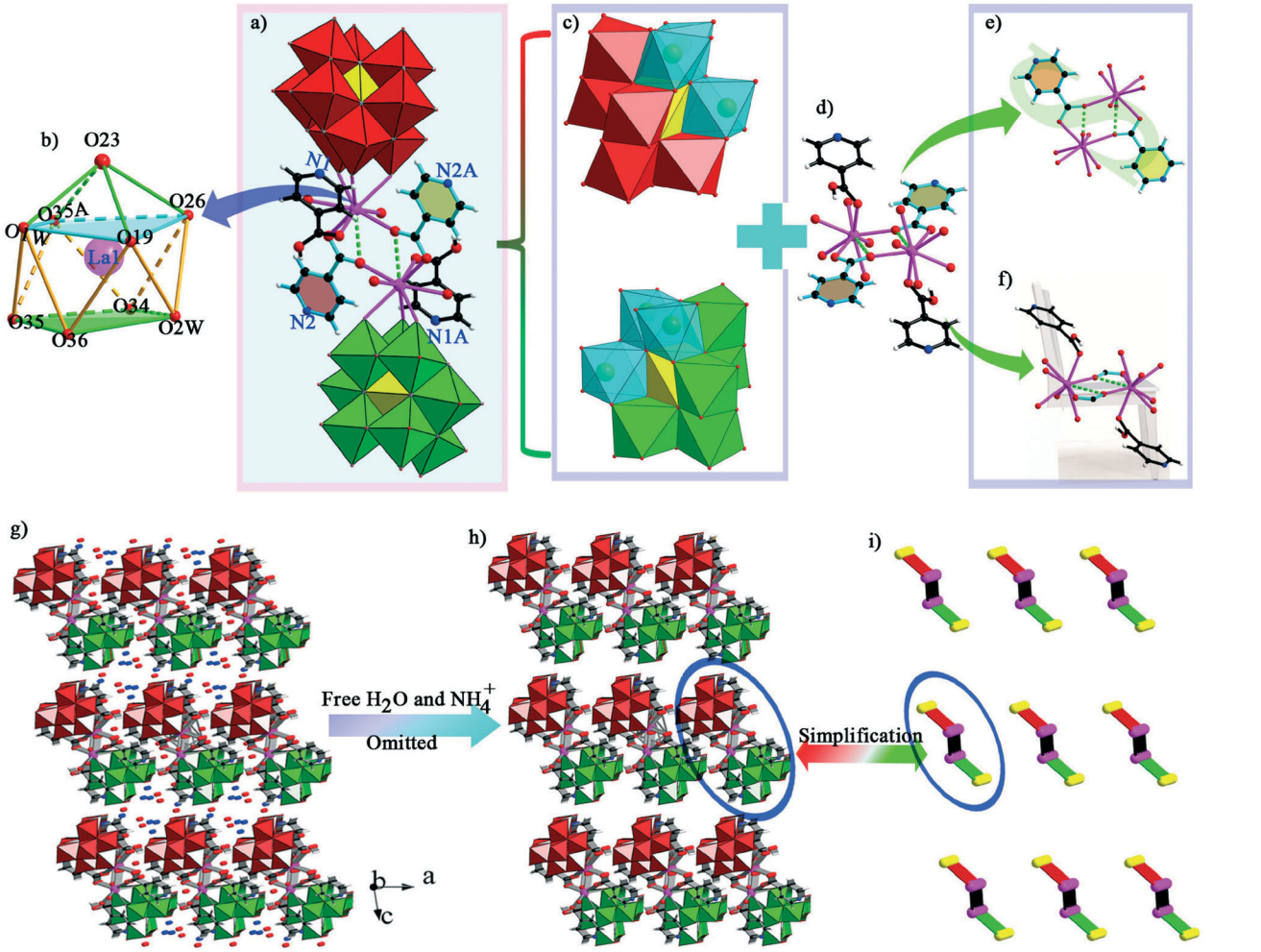

Fig. 3 (a) The inorganic–organic hybrid dimeric $\{[La(Hina)(ina)(H_2O)_2][Mn^{IV}Mo_9O_{32}]\}_2^{8-}$ core of **1**. (b) The coordination polyhedron of the $La1^{3+}$ ion. (c) Two $[MnMo_9O_{32}]^{6-}$ units in the dimeric $\{[La(Hina)(ina)(H_2O)_2][Mn^{IV}Mo_9O_{32}]\}_2^{8-}$ core of **1**. (d) The dinuclear $\{[La(Hina)(ina)(H_2O)_2]_2\}^{4+}$ cation. (e) The planar S-like structure. (f) The chair-like structure. (g) The 3-D stacking structure of **1** viewed along the *b* axis. (h) The 3-D stacking structure of **1** viewed along the *b* axis after removing dissociative NH_4^+ cations and lattice water molecules. (i) Simplified diagram of the 3-D stacking structure of **1**. The atoms with the suffix A are generated by the symmetry operation: A: $-x$, $1-y$, $1-z$.

hindrance of the ina ligands that directly leads to the elongation of the La1–O35 bond. Interestingly, two asymmetric $\{[La(Hina)(ina)(H_2O)_2][Mn^{IV}Mo_9O_{32}]\}^{4-}$ subunits are combined together by two ($\eta,^2\mu$-1,1)-Hina ligands with the La···La distance of 4.5517(8) Å, giving rise to the dimeric $\{[La(Hina)(ina)(H_2O)_2][Mn^{IV}Mo_9O_{32}]\}_2^{8-}$ polyoxoanion. It is worth noting that Hina ligands are combined with two La^{3+} ions in an especially interesting mode. Each Hina group contributes one carboxylic oxygen atom as a bridging μ_3-O atom coordinating to two La^{3+} ions and one C atom, at the same time, the other carboxylic oxygen atom serves as a bridging μ_2-O atom linking to one La^{3+} ion and one C atom. Although similar acetate-bridging dimeric polyoxoanions were previously observed in several Keggin or Dawson POMs such as $[\{(\alpha\text{-}PW_{11}O_{39})RE(H_2O)(\eta,^2\mu\text{-}1,1)\text{-}CH_3COO\}_2]^{10-}$ (RE = Sm^{3+}, Eu^{3+}, Gd^{3+}, Tb^{3+}, Ho^{3+}, Er^{3+}),[10d] $[\{(\alpha\text{-}SiW_{11}O_{39})RE(COOCH_3)(H_2O)\}_2]^{12-}$ (RE = Gd^{3+}, Yb^{3+}, Eu^{3+}, Tb^{3+}, Dy^{3+}, Ho^{3+}, Er^{3+}, Tm^{3+}),[34a,b] and $[\{La(CH_3COO)(H_2O)_2(\alpha_2\text{-}P_2W_{17}O_{61})\}_2]$,[16–34c] as far as we know, such an aromatic carboxylate-connecting Waugh-type dimeric $\{[La(Hina)(ina)(H_2O)_2][Mn^{IV}Mo_9O_{32}]\}_2^{8-}$ polyoxoanion in **1** is reported for the first time. Alternately, the hybrid dimeric $\{[La(Hina)(ina)(H_2O)_2][Mn^{IV}Mo_9O_{32}]\}_2^{8-}$ polyoxoanion of **1** can also be regarded as the fusion of two Waugh-type $[MnMo_9O_{32}]^{6-}$ units (Fig. 3c) connected by a dinuclear $\{[La(Hina)(ina)(H_2O)_2]_2\}^{4+}$ cation (Fig. 3d). In the dinuclear $\{[La(Hina)(ina)(H_2O)_2]_2\}^{4+}$ cation, two crystallographically independent La^{3+} cations are linked by two ($\eta,^2\mu$-1,1)-ina^- ligands, giving birth to a plane S-shaped structure (Fig. 3e). Moreover, each La^{3+} ion is coordinated by another pendent mono-coordinate Hina ligand, resulting in a chair-like structure (Fig. 3f). In addition, the 3-D stacking alignment of **1** along the *b* axis is illustrated in Fig. 3g, in which dissociative NH_4^+ cations and lattice water molecules are distributed in the interstices surrounded by dimeric $\{[La(Hina)(ina)(H_2O)_2][Mn^{IV}Mo_9O_{32}]\}_2^{8-}$ cores. When dissociative NH_4^+ cations and lattice water molecules are removed, it is unambiguously seen that dimeric $\{[La(Hina)(ina)(H_2O)_2][Mn^{IV}Mo_9O_{32}]\}_2^{8-}$ cores are arranged in parallel with each

other in the ac plane (Fig. 3h). Ulteriorly speaking, the packing of dimeric cores along the *b* axis can be simplified to Fig. 3i. It can be observed that dimeric cores are regularly arranged in the –AAA– mode along the *a* or the *c* axis (Fig. S3a and b in the ESI†).

10 crystallizes in the orthorhombic space group *Pbca* and its fundamental structural unit is made up of one crystallographically unique Er^{3+} cation, one classical $[MnMo_9O_{32}]^{6-}$ polyoxoanion, two Hina ligands, six coordinate water molecules, three NH_4^+ cations and seven lattice water molecules (Fig. 4a). Different from **1**, the crystallographically unique $Er1^{3+}$ cation in **10** resides in the eight-coordinate distorted bicapped trigonal prism geometry established by two carboxylate oxygen atoms (O33 and O35) from two monodentate Hina ligands [Er–O: 2.267(6)–2.320(5) Å] and six coordinate water oxygen atoms [Er–O: 2.347(6)–2.401(7) Å] (Fig. 4b). In the coordination polyhedron around the $Er1^{3+}$ cation in **10**, the O35, O3W and O5W group and the O33, O1W and O6W group constitute two bottom planes of the trigonal prism. The dihedral angle formed by two bottom planes is 17.8°. The distances of the $Er1^{3+}$ cation and two bottom planes are 1.6613 and 1.4537 Å, respectively. The O35, O1W, O3W and O6W group, the O33, O1W, O3W and O5W group and the O33, O35, O5W and O6W group form three side planes of the trigonal prism and their standard deviations from their least-square planes are 0.1890, 0.0314, and 0.1292 Å, respectively. The distances between the $Er1^{3+}$ cation and the three side planes are 1.2725, 0.7249, and 0.6163 Å, respectively. Furthermore, O2W and O4W respectively occupy the cap positions over the side planes defined by the O33, O1W, O3W and O5W group and the O33, O35, O5W and O6W group. The distance between O2W and the side plane defined by the O33, O1W, O3W, and O5W group is 1.6746 Å whereas the distance between O4W and the side plane defined by the O33, O35, O5W and O6W group is 1.7812 Å. The above-mentioned data indicate that the bicapped trigonal prism is highly distorted. Comparing **10** with **1**, although **1** and **10** consist of the $[MnMo_9O_{32}]^{6-}$ polyoxoanion, the RE-organic cations in them are different: (a) the coordination number of the $La1^{3+}$ cation in **1** is nine-coordinate and the $La1^{3+}$ cation inhabits in the monocapped square antiprismatic geometry (Fig. 4c) while the coordination number of the $Er1^{3+}$ cation in **10** is eight-coordinate and the $Er1^{3+}$ cation is embedded in the bicapped trigonal prism geometry (Fig. 4d); (b) the bridging ina^- ligand

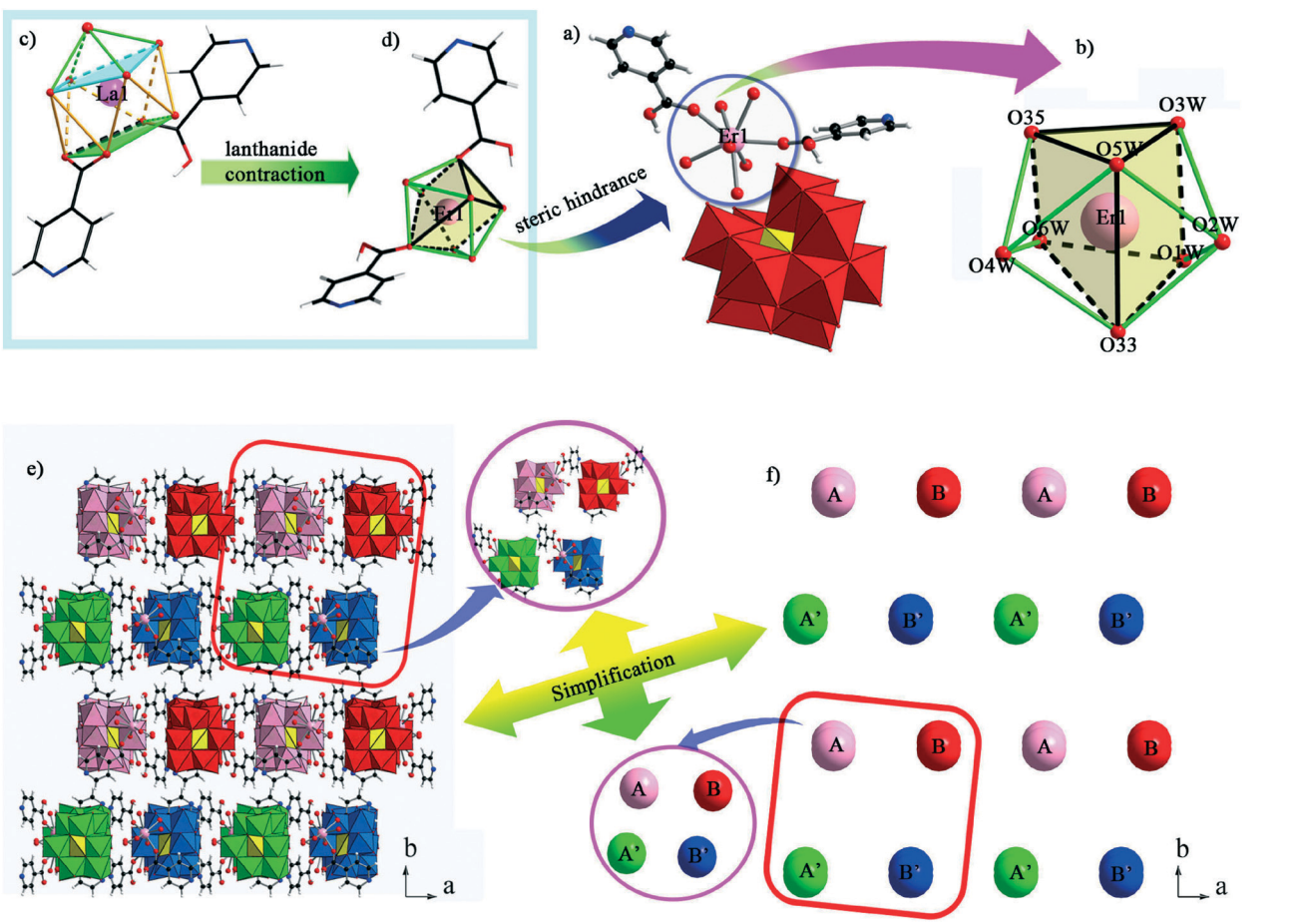

Fig. 4 (a) The fundamental structural unit of **10**. Free water molecules and ammonia ions are omitted for clarity. (b) The coordination geometry of the $Er1^{3+}$ ion. (c) The coordination environment of the $La1^{3+}$ ion in **1**. (d) The coordination environment of the $Er1^{3+}$ ion in **10**. (e) The 3-D packing structure of **10** viewed along the *c* axis. (f) Simplified diagram of 3-D packing structure of **10** viewed along the *c* axis.

in **1** adopts the (η,$^2\mu$-1,1) coordination mode and the pendant Hina ligand in **1** shows the monodentate coordination mode whereas two pendant Hina ligands in **10** employ the monodentate coordination mode. It should be pointed out that the coordination number of the RE^{3+} cations in **1** and **10** transforms from 9 to 8 primarily because of the effect of lanthanide contraction and the different coordination modes of Hina ligands. Actually, a similar phenomenon that the effect of lanthanide contraction leads to the difference of structures has been encountered in our previous work.[26a] Furthermore, the molecular structural units of **10** are regularly aligned to give rise to the interesting 3-D packing structure (Fig. 4e). As we can see from the 3-D packing structure, neighboring molecular structural units are arranged in different fashions to reduce the steric hindrance as much as possible, which helps to enhance the chemical stability of **10**. Moreover, in order to clearly understand the 3-D structure of **10**, the structural units are simplified into different color spheres and the structural units with different orientations are labeled with A, B, A′ and B′. Thus, the packing of **10** along the *c* axis can be simplified to the structure in Fig. 4f. It can be seen that the molecular structural units are regularly arranged in the –ABA′B′– mode along the axis and in the –AA′AA′– or –BB′BB′– mode along the *b* axis.

From the above-mentioned structural discussion, it can be concluded that the key reason for the different structures of **1–3** (type I) and **4–13** (type II) is closely related to the lanthanide contraction effect although their synthetic conditions are almost the same. As illustrated in Table S2 in the ESI,† when the ionic radii of RE^{3+} ions are larger than 0.980 Å, type I is obtained. On the contrary, when the ionic radii of RE^{3+} ions are smaller than 0.980 Å, type II is separated. Obviously, across the series of RE^{3+} ions from La^{3+} to Yb^{3+}, the decrease of the ionic radii of RE^{3+} ions makes the coordination number of RE^{3+} ions become smaller from nine to eight. Since the ionic radius of the Y^{3+} ion lies between Tm^{3+} and Yb^{3+}, its species belongs to type II. In the structure of type I, the nine-coordinate distorted monocapped square antiprismatic geometry of the RE^{3+} ion renders the RE^{3+} ion to coordinate with three terminal oxygen (O19, O23, O26) atoms of the Waugh-type $[MnMo_9O_{32}]^{6-}$ polyoxoanion and the longer RE–O bond lengths (herein the RE–O average bond length $>$ 2.50 Å) can make two neighboring RE^{3+} ions combine together, thus constructing the hybrid dimeric $\{[RE(Hina)(ina)(H_2O)_2][Mn^{IV}Mo_9O_{32}]\}_2^{8-}$ core. Furthermore, the (η,$^2\mu$-1,1) coordination mode of the ina^- ligand in type I can also reinforce the stability of the dimeric assembly. However, in the structure of type II, the eight-coordinate bicapped trigonal prism geometry cannot entail the three terminal oxygen atoms in the structure of type I to effectively bind with the RE^{3+} ion. Moreover, the shorter RE–O bond lengths (herein the RE–O average bond length $<$ 2.50 Å) make the combination of two neighboring RE^{3+} ions become unfavorable. These two common actions result in the separation of the $[RE(Hina)_2(H_2O)_6]^{3+}$ cation and the $[MnMo_9O_{32}]^{6-}$ polyoxoanion in the structure of type II. Such a phenomenon that the lanthanide contraction effect leads to the structural discrepancy of the anticipated compounds was previously encountered.[26]

UV-visible spectra and diffuse reflectance spectra

Because **1–3** are isostructural and **4–13** also are isomorphic, only the UV spectra of **3** and **8** as representatives were measured in aqueous solution. As illustrated in Fig. S4a and b in the ESI,† the UV spectral profiles of **3** and **8** in aqueous solution are almost the same in the range of 400–200 nm, suggesting that both **3** and **8** consist of the same polyoxoanion skeleton, which is in good consistency with the results of IR and single-crystal X-ray diffraction analysis. The UV spectra of **3** and **8** all display two characteristic absorption peaks derived from the Waugh-type polyoxoanion so that the strong absorption band at 206 nm for **3** and 207 nm for **8** can be assigned to the pπ–dπ charge-transfer transitions of the $O_t \rightarrow Mo$ bonds and the weak one at 233 nm for **3** and 232 nm for **8** is attributed to the pπ–dπ charge-transfer transition of the $O_b \rightarrow Mo$ bonds.[28a] It is well known that POMs are extremely sensitive to the pH variation of the studied medium. Consequently, in order to examine the influence of pH on their stability in aqueous solution, the UV spectra of **3** and **8** in aqueous solution at various pH values have been carefully explored. The pH values in the alkaline region and the acidic region are adjusted by using diluted NaOH or diluted HCl solution. When **3** is dissolved in water, the pH of the aqueous solution is 4.3. As you can see from Fig. S4c in the ESI,† when the pH drops from 4.3 to 2.4, no obvious variation is observed in the UV spectra of **3**. On further decreasing the pH, the $O_b \rightarrow Mo$ absorption band at 233 nm will gradually disappear and a new band at 270 nm appears and becomes more and more obvious, which manifests that the structure of the $[MnMo_9O_{32}]^{6-}$ polyoxoanion begins to change. Correspondingly, as the pH increases from 4.3 to 5.0, the evolution of the UV spectra is unapparent. When the pH is higher than 5.0, the $O_t \rightarrow Mo$ absorption band at 206 nm will gradually disappear (Fig. S4d in the ESI†). It can be concluded from the above analysis that **3** is stable in aqueous solution in the pH range of about 2.4–5.0. Analogously, as revealed in Fig. S4e and f in the ESI,† **8** is stable in the pH range of *ca.* 2.3–5.0. In addition, the UV spectral evolution of **3** and **8** in aqueous solution with time has been measured (Fig. S5 in the ESI†), which indicates that **3** and **8** can be stable for at least four days. In addition, the visible spectra of $(NH_4)_6[MnMo_9O_{32}]\cdot 8H_2O$, **3** and **8** have also been measured in aqueous solution (Fig. S6 in the ESI†), which all exhibit a wide absorption band centered at *ca.* 478 nm that can be attributed to the $^4T_{2g} \rightarrow {}^4A_{2g}$ transitions of the Mn^{4+} center in the $[MnMo_9O_{32}]^{6-}$ polyoxoanion.[35] To obtain the optical band gaps of **3** and **8**, the optical diffuse reflectance spectra for their powdered crystal samples and $(NH_4)_6[MnMo_9O_{32}]\cdot 8H_2O$ were measured. The optical band gap (E_g) can be determined by the intersection point between the energy axis and the line extrapolated from the linear portion of the absorption edge

in a plot of Kubelka–Munk function against energy E.[36a,b] The Kubelka–Munk function, $a/S = (1 - R)^2/2R$, can be converted from the diffuse reflectance data, where a is the absorption coefficient, S is the scattering coefficient, and R is the reflectance of an infinitely thick layer at a given wavelength. Plots of Kubelka–Munk function *versus* energy E (eV) for **3**, **8** and $(NH_4)_6[MnMo_9O_{32}]\cdot 8H_2O$ are illustrated in Fig. S7 in the ESI,† from which E_g can be calculated as E_g = 2.10 eV, 2.12 eV and 2.03 eV for **3**, **8** and $(NH_4)_6[MnMo_9O_{32}]\cdot 8H_2O$, respectively, suggesting that they exhibit a semiconductor-like characteristic. The optical band gaps are involved in the energy-level difference between the oxygen p-type HOMO and the molybdenum p-type LUMO.[32e,36c] Obviously, the intensive explorations of the influence of the pH variation on their stability in aqueous solution, the UV spectral evolution with time and the optical diffuse reflectance spectra provide the important prerequisites for investigating their photocatalytic properties.

Photocatalytic properties

Azo dyes constitute the largest class of the overall category of industrial dye stuffs, which are extensively used in industries such as textiles, leather, paper, printing, plastic, and so on.[37] Most of them are toxic, carcinogenic, nonbiodegradable and harmful to the human living environment, human health and aquatic life, giving rise to an increasing and serious threat all over the world.[38a] As a consequence, relevant investigations on the degradation of azo dyes involving different degradation techniques have drawn considerable attention.[37a,38b–e] In recent years, the photochemistry and photocatalysis of POM-based inorganic–organic hybrid materials have aroused increasing interest, which could decompose organic pollutants into pollution-free small molecules such as small organic acids and CO_2.[39] Herein, we selected azophloxine as a model pollutant of azo dye contaminants in water to evaluate the photocatalytic effectiveness of **1–13** as catalysts.

The influence of different pH on the photocatalytic activities of 3 and 8 under 300 W mercury lamp irradiation

Because **1–3** and **4–13** are respectively isostructural, the photocatalytic degradation properties of only **3** and **8** as representatives are systematically explored. As we all know, the pH of the photocatalytic system is also an important parameter for optimizing the operational conditions since the pH of the dye solution system will influence the hydroxyl radical concentration, the charge of the molecule, adsorption/desorption of the dye molecule and its intermediates onto a photocatalyst surface and the surface charge property of the photocatalyst.[40] According to the above-mentioned experimental results about the influence of pH on the stability of **3** and **8** in aqueous solution by means of UV spectroscopy, **3** and **8** are stable in the pH range of *ca.* 2.4–5.0 and 2.3–5.0, respectively. Therefore, photocatalytic degradation reactions for **3** and **8** were preliminarily carried out under 300 W mercury lamp irradiation at the initial azophloxine concentration of 6 × 10^{-5} mol L^{-1} with 9.8 × 10^{-6} mol (based on $[MnMo_9O_{32}]^{6-}$) catalyst in the dye aqueous solution volume of 50 mL at room temperature and constant stirring, and three selected pH values ranging from 4.4 to 2.6 (the pH was adjusted by dilute hydrochloric acid solution or dilute sodium hydroxide solution) were investigated. Furthermore, for comparison, the photocatalytic degradation experiment of the azophloxine solution (6 × 10^{-5} mol L^{-1}) without any photocatalyst was also carried out with an initial pH of 6.1 and 2.6. The conversion of azophloxine in this reaction was quantified by the measurement of the decay of absorbance of its characteristic absorption band at around 504 nm as a function of time. The conversion of azophloxine in this reaction was quantified by the measurement of the decay of absorbance of its characteristic absorption band at around 504 nm as a function of time. Moreover, the plots of the conversion of azophloxine can be expressed as $y = (C_0 - C_t)/C_0$, in which C_0 represents the absorbance of the characteristic absorption band of azophloxine at around 504 nm at the initial time (t = 0) and C_t is the absorbance of the characteristic absorption band of azophloxine at a given time (t). The relevant measurement results are depicted in Fig. 5.

As seen in Fig. 5a and b, after the azophloxine solutions without any catalyst with initial pH = 6.1 and pH = 2.6 are exposed to 300 W mercury lamp irradiation for 2 h at room temperature, the conversion of azophloxine is about 20% and 40%, respectively. Obviously, the low pH can be conducive to the degradation of azophloxine. In the presence of **3** (Fig. 5c–e), it can be observed from Fig. 5f that 56% and 70% azophloxine degradation occurs within 2 h at pH = 4.4 and pH = 3.8 whereas 95% azophloxine degradation can be achieved within 2 h at pH = 2.6. It is very clear that dye degradation and color removal are maximum at pH = 2.6. The degradation experiments of **8** are similar to those of **3** (Fig. 5g–j). With the decrease of the pH, dye degradation and color removal speed up probably because strong attractive forces between dye molecules and the catalyst surface cause a high rate of adsorption of dye onto the catalyst surface and consequently high degradation and color removal.[40a]

Furthermore, under the conditions with the optimum pH = 2.6, the photocatalytic degradation reactions for **1–2**, **4–7** and **4–13** (Fig. S8a–j in the ESI†) were also measured under 300 W mercury lamp irradiation under the same conditions as **3** and **8**. The obvious decrease of absorbance of the characteristic absorption band is seen after irradiation, signifying an obvious degradation of the dye. These results reveal that **1–2**, **4–7** and **4–13** as catalysts have apparent photocatalytic activities towards the degradation of azophloxine. It is noteworthy that **1–2**, **4–7** and **4–13** exhibit similar photocatalytic activities towards the degradation of azophloxine under UV irradiation, which might be because they consist of $[MnMo_9O_{32}]^{6-}$ polyoxoanions. In order to consolidate the conclusion, the photocatalytic degradation experiment with $(NH_4)_6[MnMo_9O_{32}]\cdot 8H_2O$ as the catalyst has been also carried out under the same conditions (Fig. S8l in the ESI†). The

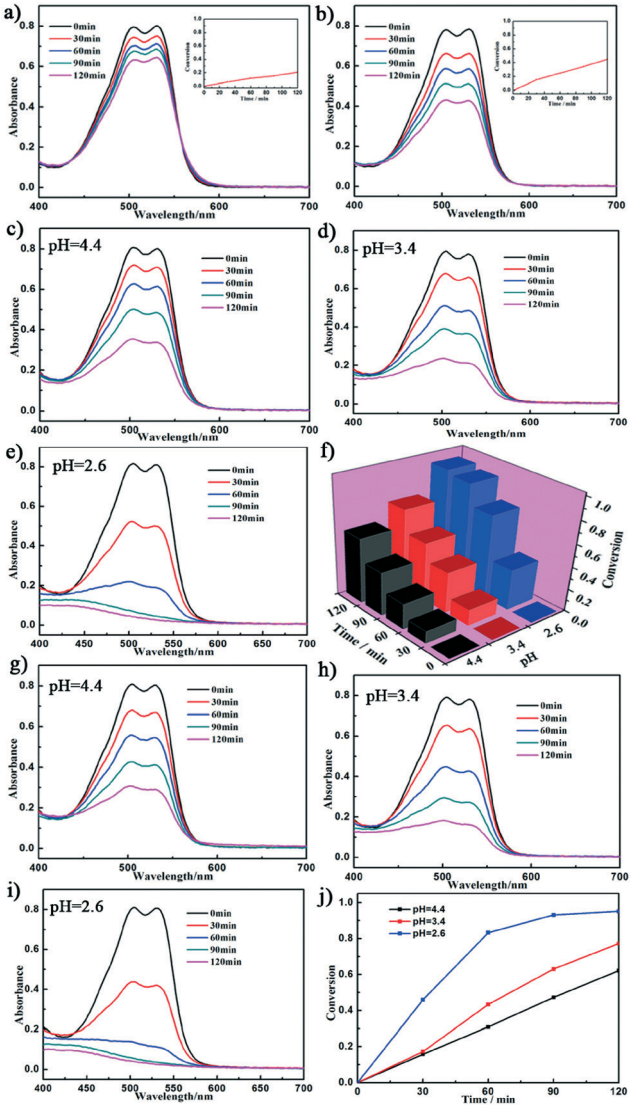

Fig. 5 UV-visible absorption spectral changes for the azophloxine solutions at various irradiation times: (a) without any catalyst with initial pH = 6.1; (b) without any catalyst with pH = 2.6; (c) in the presence of **3** (20 mg) with pH = 4.4; (d) in the presence of **3** (20 mg) with pH = 3.4; (e) in the presence of **3** (20 mg) with pH = 2.6; (f) the effect of the different pH on the conversion of azophloxine for **3**; (g) in the presence of **8** (20.8 mg) with pH = 4.4; (h) in the presence of **8** (20.8 mg) with pH = 3.4; (i) in the presence of **8** (20.8 mg) with pH = 2.6; (j) the effect of the different pH on the conversion of azophloxine for **8**. Inset: the conversion of azophloxine (y) with reaction time (t). Experimental conditions: initial concentration of azophloxine: 6×10^{-5} mol L^{-1}, dye solution volume: 50 mL, catalyst amount: 9.8×10^{-6} mol (based on $[MnMo_9O_{32}]^{6-}$).

results demonstrate that $(NH_4)_6[MnMo_9O_{32}]\cdot 8H_2O$ shows evident photocatalytic activity towards the degradation of azophloxine. As a result, the $[MnMo_9O_{32}]^{6-}$ polyoxoanions play an important role during the course of the photocatalytic experiments of **1–13**. In line with previous studies,[37a,38b,c,41] the decoloration process may be related to the cleavage of the azo group of azophloxine. Therefore, in the subsequent photocatalytic tests, **3** and **8** are selected as the representative

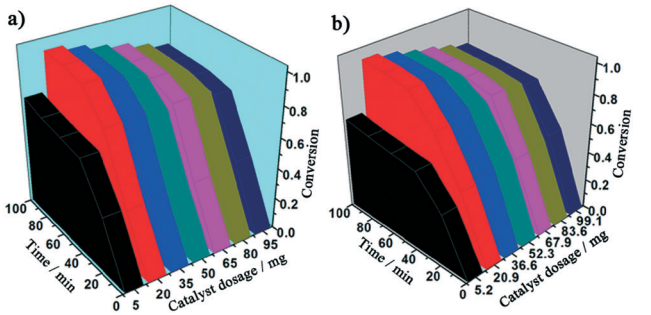

Fig. 6 Effect of the catalyst dosage of **3** (a) and **8** (b) on the conversion of azophloxine. Experimental conditions: dye solution volume: 50 mL, initial concentration of azophloxine: 6×10^{-5} mol L^{-1}, pH = 2.6.

photocatalysts to explore the influence of the catalyst dosage, the molar ratio of the doped VK-TA18-TiO_2 and the different irradiation sources on the photocatalytic activities.

The influence of the catalyst dosage on the photocatalytic activities of 3 and 8 under 300 W mercury lamp irradiation

It is well known that the catalyst dosage is one of the most important parameters in the photodegradation of organic compounds. Therefore, the effect of the catalyst dosage on the photodegradation of azophloxine was probed by varying the dosage of **3** and **8** from 2.46×10^{-6} mol to 4.67×10^{-5} mol (based on $[MnMo_9O_{32}]^{6-}$, **3**: 5–95 mg; **8**: 5.2–99.1 mg) in 6×10^{-5} mol L^{-1} of the employed solutions of azophloxine and the results are displayed in Fig. 6 and S9 in the ESI.† The results indicate that the conversion gradually increases with increasing catalyst dosage of **3** and **8** from 2.46×10^{-6} mol to 9.82×10^{-6} mol. However, the photodegradation efficiency decreases slightly with increasing catalyst dosage from 9.82×10^{-6} mol to 4.67×10^{-5} mol. Apparently, the optimal catalyst dose is 9.82×10^{-6} mol, the main reason for which is that the photocatalytic activity is found to be dependent on the initial catalyst concentration because the number of total active sites increases with the increase of the catalyst dosage and more catalytic active sites can lead to the enhancement of the photocatalytic activity. However, the conversion decreases when the photocatalyst dosage is higher than 9.82×10^{-6} mol because of the increased light scattering effects of the photocatalysts.[42]

The influence of various molar ratios of the doped VK-TA18-TiO_2 : 8 on the conversion of azophloxine under 300 W mercury lamp irradiation

Titanium dioxide may be a promising photocatalyst because of some of its important advantages including low cost, higher stability, non-toxicity and enormous efficiency in degrading various organic contaminants in the field of sewage treatment.[43a–e] TiO_2-based materials have been demonstrated to be one of the most reliable heterogeneous photocatalysts and are most widely activated under UV light irradiation.[38c,43f] To date, some photocatalysis investigations

involving POM–TiO_2 composite materials have been performed in the past decade because POMs are a family of green and stable early transition metal-oxo clusters that display semiconductor-like photochemical behavior owing to similar electronic characteristics (band gap transition for semiconductors and HOMO–LUMO transitions for POMs).[38c,44] The role of the POM in TiO_2 photocatalysis is crucial in enhancing the overall photoefficiency by retarding the fast recombination of a charge-pair (h^+–e^-) on TiO_2 and producing a strong oxidant O_2^- and $OH^\cdot$ radicals.[44b] Therefore, we chose the VK-TA18 nanometer titanium dioxide (denoted as VK-TA18-TiO_2) as the dopant to improve the degradation efficiency of **3** and **8** towards azophloxine. As shown in Fig. 7 and S10 in the ESI,† based on 9.82×10^{-6} mol (based on $[MnMo_9O_{32}]^{6-}$) **3** (20 mg) and **8** (20.9 mg), the molar ratio of VK-TA18-TiO_2 : **3**/**8** varies between 1 : 2 and 4 : 1 with the azophloxine concentration of 6×10^{-5} mol L^{-1} and the effect of the doping amount of VK-TA18-TiO_2 on the conversion of azophloxine was measured. The results show that the conversion within 80 min increases dramatically with increasing doping amount of VK-TA18-TiO_2 from 0 to 1 : 2, which may be ascribed to the synergistic effect resulting from the combination of manganomolybdates and VK-TA18-TiO_2. It is hypothesized that the interfacial electron transfer takes place from the conduction band of VK-TA18-TiO_2 to $[MnMo_9O_{32}]^{6-}$ units upon UV light irradiation and this effective electron transfer can bridle fast electron–hole recombination in VK-TA18-TiO_2 and the trapped holes have sufficient time to react with H_2O to generate $OH^\cdot$ radicals.[38c,44b] Specifically, with increasing VK-TA18-TiO_2, the band gap of the mixture (**3**, **8** and VK-TA18-TiO_2) becomes narrow, which gives a higher population of the photoexcited electrons and holes to participate in the photocatalytic reaction. Thus, more available and active sites on the catalyst surfaces can be produced, which are responsible for the destruction of azophloxine.[45a] However, with a continuous increase of the doping amount of VK-TA18-TiO_2, no significant enhancement in the conversion is observed, which may be because the total active surface areas increase with the increase of VK-TA18-TiO_2 dosage; at the same time, the turbidity of the suspension also increases with the addition of a high dose of VK-TA18-TiO_2, which results in the decrease of the penetration of UV light and the aggregation of photocatalysts and hence no remarkable enhancement in the conversion is observed.[45b] That is to say, a higher dose of catalyst may not be useful in consideration of both aggregation of photocatalysts and reduced irradiation field owing to light scattering effects.[45b] It can be clearly seen from Fig. 7 that the optimal molar ratio of VK-TA18-TiO_2 : **3**/**8** is 1 (0.4 mg VK-TA18-TiO_2) : 2.

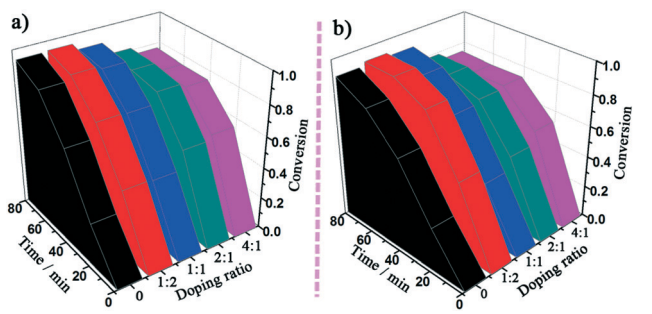

Fig. 7 Effects of various molar ratios of the doped VK-TA18-TiO_2 : **3** (a) and VK-TA18-TiO_2 : **8** (b) on the conversion of azophloxine. Experimental conditions: initial concentration of azophloxine: 6×10^{-5} mol L^{-1}, dye solution volume: 50 mL, pH = 2.6.

The influence of different irradiation sources on the photocatalytic activities of 3 and 8

The influence of different irradiation sources (300 W mercury lamp and 500 W xenon lamp) on the photocatalytic activities of **3** and **8** was investigated. On the basis of the above results, the optimum experimental conditions (the catalyst ratio of VK-TA18-TiO_2 : **3**/**8** is 1 : 2 [0.4 mg VK-TA18-TiO_2 and 9.82×10^{-6} mol **3** or **8** (based on $[MnMo_9O_{32}]^{6-}$, 20 mg **3** or 20.9 mg **8**)], the concentration of azophloxine is 6×10^{-5} mol L^{-1} and pH is 2.6) were selected. As shown in Fig. 8 and S11 in the ESI,† we found that VK-TA18-TiO_2 : **3**/**8** = 1 : 2 at pH = 2.6 is more photoactive than other catalysts under various irradiation sources. For instance, after irradiation for 80 min under the UV light of a 300 W mercury lamp, the conversions of azophloxine are 46%, 92% and 94% for 0.4 mg VK-TA18-TiO_2, 20 mg **3**, the mixed phase of 20 mg **3** and 0.4 mg VK-TA18-TiO_2, and 90%, 95% for 20.9 mg **8**, the mixed phase of 20.9 mg **8** and 0.4 mg VK-TA18-TiO_2, respectively. In contrast, after irradiation for 100 min under the visible light of a 500 W xenon lamp, the conversions of azophloxine are 16%, 35% and 45% for 0.4 mg VK-TA18-TiO_2, 20 mg **3**, the mixed phase of 20 mg **3** and 0.4 mg VK-TA18-TiO_2, and 38%, 46% for 20.9 mg **8**, the mixed phase of 20.9 mg **8** and 0.4 mg VK-TA18-TiO_2, respectively. These results indicate that the optimum

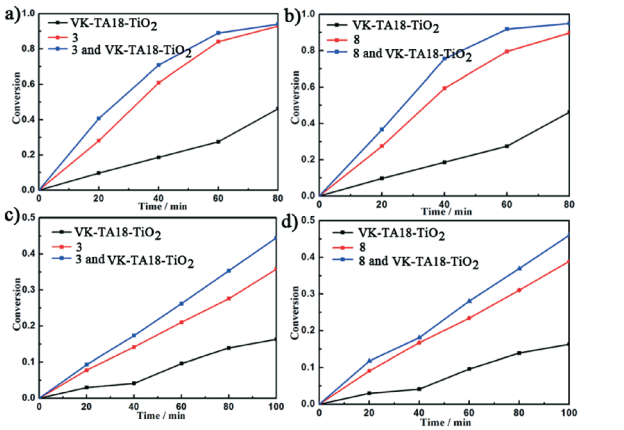

Fig. 8 (a) Conversion of azophloxine with reaction time under a 300 W mercury lamp light for **3**. (b) Conversion of azophloxine with reaction time under a 300 W mercury lamp light for **8**. (c) Conversion of azophloxine with reaction time under a 500 W xenon lamp light for **3**. (d) Conversion of azophloxine with reaction time under a 500 W xenon lamp light for **8**.

conditions are the combination of pH = 2.6 and the mixed phase of 9.82×10^{-6} mol **3** or **8** (based on $[MnMo_9O_{32}]^{6-}$, 20 mg **3** or 20.9 mg **8**)] and 0.4 mg VK-TA18-TiO_2 under either the UV light of a 300 W mercury lamp or the visible light of a 500 W xenon lamp, which can be attributed to the synergistic effect of **3**/**8** and VK-TA18-TiO_2. This synergistic effect is that (a) **3** and **8** have very photochemical characteristics of the semiconductor photocatalysts (this has been proved by the result of the optical diffuse reflectance spectrum) and (b) **3** and **8** have empty d orbits and can be used as good electron acceptors. Thus, in the photocatalytic mixed phase system of **3**/**8** and VK-TA18-TiO_2, the fast charge-pair (e^-–h^+) recombination on the surface of VK-TA18-TiO_2 can be delayed because the electrons are transferred into the empty d orbits of **3**/**8**, which is in agreement with previous documents.[46] As a result, the photocatalytic mixed phase system of **3**/**8** and VK-TA18-TiO_2 has a high photocatalytic activity. Moreover, the photocatalytic activity of the mixed phase system of **3**/**8** and VK-TA18-TiO_2 under UV light is slightly higher than that under visible light. And no obvious decay of absorbance of the characteristic absorption band at around 504 nm is observed under the visible light of a 500 W xenon lamp, which indicates that the azophloxine solution is not self-degraded.

Photoluminescence (PL) properties

RE-containing materials have always played a remarkable role in lighting and light conversion technologies such as light emitting diodes, lasers, NIR-emitting materials, cathode-ray and plasma displays,[47] which are mainly related to the electronic properties of the RE ions including the good shielding of the 4f orbitals by the filled $5s^25p^6$ subshells resulting in well-defined absorption and emission bands and high color purity.[48] Hence, the atomic characteristics of RE cations are usually maintained in the RE-containing materials. Thus, some luminescent RE-based POMs have been addressed.[49] Herein, the PL properties and lifetime decay behaviors of solid-state samples of **3** (near-IR luminescence), **4** and **5** (UV-visible luminescence) have been investigated at room temperature, respectively.

UV-visible luminescence. **4** emits an obvious red fluorescence upon excitation with an ultraviolet light of 340 nm. The emission spectrum of **4** displays four typical emission peaks between 500 and 800 nm. The three emission bands appearing at 562 nm, 597 nm and 644 nm are attributed to the $^4G_{5/2} \rightarrow {}^6H_{5/2}$, $^4G_{5/2} \rightarrow {}^6H_{7/2}$ and $^4G_{5/2} \rightarrow {}^6H_{9/2}$ transitions of the Sm^{3+} cation, respectively (Fig. 9a).[50] To clarify and comprehend the broad and strong emission band centered at 705 nm (Fig. 9b), the PL emission of $(NH_4)_6[MnMo_9O_{32}]\cdot 8H_2O$ has also been studied. Upon excitation at 340 nm, $(NH_4)_6[MnMo_9O_{32}]\cdot 8H_2O$ exhibits a strong emission band at 710 nm (Fig. S12a in the ESI†), which is mainly induced by the $^2E \rightarrow {}^4A_2$ transition of the Mn^{4+} cation in the $[MnMo_9O_{32}]^{6-}$ units.[51] Comparing the PL spectrum of **4** with that of $(NH_4)_6[MnMo_9O_{32}]\cdot 8H_2O$, evidently, the broad and strong emission band centered at 705 nm in **4** can be assigned to the $^2E \rightarrow {}^4A_2$ transition of the Mn^{4+} cation in the $[MnMo_9O_{32}]^{6-}$ fragment. In addition, the stark splitting of the $^4G_{5/2} \rightarrow {}^6H_{7/2}$ transition is attributed to the low local symmetry of the Sm^{3+} ion,[52] which is well consistent with the result (the Sm^{3+} ion inhabits in an eight-coordinate distorted bicapped trigonal prism geometry) of the single-crystal structure analysis for **4**. In addition, by monitoring the emission at 705 nm, the excitation spectrum of **4** has been collected (Fig. 9c). The excitation spectrum is dominated by a strong band at 340 nm, which is assigned to the O → Mo ligand-to-metal charge transfer (LMCT) transition.[51a] This observation further consolidates that photoexcitation of the O–Mo LMCT band results in an intramolecular energy transfer from the O–Mo LMCT triplet state into Sm^{3+} and Mn^{4+} cations, followed by the luminescence of the $^4G_{5/2} \rightarrow {}^6H_{5/2}$, $^4G_{5/2} \rightarrow {}^6H_{7/2}$ and $^4G_{5/2} \rightarrow {}^6H_{9/2}$ transitions of the Sm^{3+} cation and the $^2E \rightarrow {}^4A_2$ transition of the Mn^{4+} cation. Similar procedures have been observed by Yamase *et al.* in the sensitized luminescence Eu^{3+}, Mn^{4+} and Cr^{3+} POMs as a result of intramolecular energy transfer.[49a] In order to determine the lifetime, the luminescence decay curve of **4** has been measured by monitoring the excitation at 340 nm and the most intense emission at 705 nm (Fig. 9d), which can be well fitted with a second-order exponential function $I = A_1\exp(-t/\tau_1) + A_2\exp(-t/\tau_2)$, where I is the luminescence intensity, A_1 and A_2 are the pre-exponential factors, t is the time, and τ_1 and τ_2 are the fast and slow components of the luminescence lifetimes. The fitted luminescence lifetimes τ_1 and τ_2 are 1.40 μs (37.46%) and 9.49 μs (62.54%), and the pre-exponential factors A_1 and A_2 are 3548.94 and 872.89, respectively. Thus, the average decay times (τ^*) can be determined by the following formula: $\tau^* = (A_1\tau_1^2 + A_2\tau_2^2)/(A_1\tau_1 + A_2\tau_2)$.[53] Therefore, its average lifetime is calculated to be 6.46 μs. Nevertheless, from the crystal structure of **4**, we can know that there is one crystallographically unique $[MnMo_9O_{32}]^{6-}$ fragment in **4**, and it is almost impossible that there are two different lifetimes for one crystallographically unique $[MnMo_9O_{32}]^{6-}$ fragment in **4**. To further investigate the reason for the two different lifetimes, the luminescence decay curve of the $(NH_4)_6[MnMo_9O_{32}]\cdot 8H_2O$ (Fig. S12c in the ESI†) has been also recorded under similar conditions to **4** and can be fitted to a single exponential function: $I = A\exp(-t/\tau)$ with τ of 11.21 μs. This experimental result indicates that the lifetime of **4** indeed originates from the combined contributions of the Sm^{3+} ion and the $[MnMo_9O_{32}]^{6-}$ fragment. The solid-state emission spectrum of **5** under excitation at 340 nm displays four obvious emission peaks at 579 nm, 593 nm, 615 nm and 702 nm (Fig. 9e and f). The three typical emission peaks at 579, 593 and 615 nm are respectively attributed to the $^5D_0 \rightarrow {}^7F_0$,$^5D_0 \rightarrow {}^7F_1$ and $^5D_0 \rightarrow {}^7F_2$ transitions of the Eu^{3+} ion,[48b,54] whereas another peak at 702 nm is derived from the $^2E \rightarrow {}^4A_2$ transition of the Mn^{4+} cation in the $[MnMo_9O_{32}]^{6-}$ units.[51] In addition, the symmetry-forbidden emission $^5D_0 \rightarrow {}^7F_0$ is seen at 579 nm, which reveals that the Eu^{3+} cation in **5** inhabits in the low symmetrical coordination environment.[54,55] It is well known that the $^5D_0 \rightarrow {}^7F_2$ transition induced by the electric dipole moment

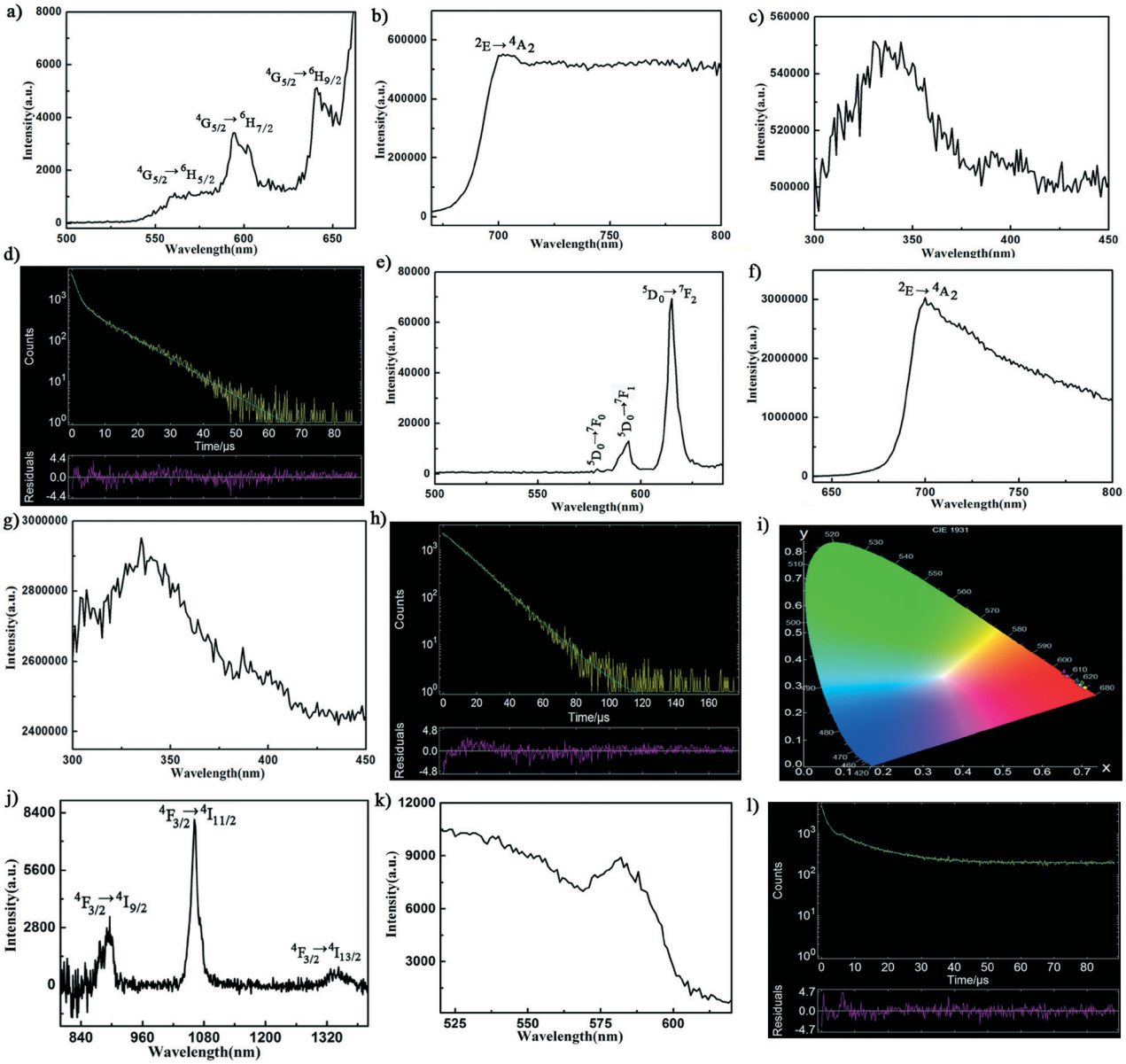

Fig. 9 (a) The emission spectrum between 500 nm and 650 nm of **4** under excitation at 340 nm at room temperature. (b) The emission spectrum between 650 nm and 800 nm of **4** under excitation at 340 nm at room temperature. (c) The excitation spectrum of **4** obtained by monitoring the emission at 705 nm. (d) The luminescence decay curve of **4**. (e) The emission spectrum between 500 nm and 650 nm of **5** under excitation at 340 nm at room temperature. (f) The emission spectrum between 650 nm and 800 nm of **5** under excitation at 340 nm at room temperature. (g) The excitation spectrum of **5** obtained by monitoring the emission at 703 nm. (h) The luminescence decay curve of **5**. (i) CIE chromaticity diagram of the emissions of **0**, **4**, and **5**. (j) NIR emission spectrum of **3** under excitation at 581 nm at room temperature. (k) NIR excitation spectrum of **3** obtained by monitoring the emission at 1062 nm. (l) The luminescence decay curve of **3**.

is hypersensitive to the coordination environment of the Eu^{3+} ion, whereas the $^5D_0 \rightarrow {}^7F_1$ transition is a magnetic dipole in origin and less sensitive to its environment.[56] Generally speaking, the magnetic dipole $^5D_0 \rightarrow {}^7F_1$ transition is regnant in a centrosymmetric coordination environment; in contrast, the electronic dipole $^5D_0 \rightarrow {}^7F_2$ transition is usually the strongest emission band in a ligand field without inversion symmetry.[57] The intensity ratio of the $I(^5D_0 \rightarrow {}^7F_2)/I(^5D_0 \rightarrow {}^7F_1)$ can be used as a criterion to check the symmetry of the local environment of the Eu^{3+} ion.[48b] In the case of **5**, the intensity ratio of the $I(^5D_0 \rightarrow {}^7F_2)/I(^5D_0 \rightarrow {}^7F_1)$ is equal to about 3.5, which also implies that the Eu^{3+} ion resides in the low symmetric coordination environment. This conclusion is supported by the case that the crystallographically independent Eu^{3+} ion in **5** exhibits the eight-coordinate distorted bicapped trigonal prism geometry. To further determine the lifetime, the luminescence decay curve of **5** has also been recorded (Fig. 9h), which can be well fitted to a single exponential function, $I = A\exp(-t/\tau)$, yielding the lifetime value τ of 13.65 μs and the pre-exponential factor A of 2417.29. In

comparison with the luminescence decay curve of the $(NH_4)_6[MnMo_9O_{32}]\cdot 8H_2O$ (Fig. S12c in the ESI†) with a single exponential function affording τ of 11.21 μs, it can be concluded that the luminescence lifetime of **5** primarily originates from the contribution of the $[MnMo_9O_{32}]^{6-}$ fragment.

A better understanding of the true color is fairly vital in the domains of lighting and display devices.[58] The CIE 1931 diagram is widely used to examine all the possible colors by combining three primary colors, in which the chromaticity coordinates *x* and *y* are used for ascertaining the accurate emission colors of the as-synthesized materials. The CIE chromaticity coordinates for **4**, **5** and $(NH_4)_6[MnMo_9O_{32}]\cdot 8H_2O$ (**0**) are determined based on their matching emission spectra and are calculated as (0.66292, 0.33629), (0.69578, 0.30272) and (0.70754, 0.29232), respectively (Fig. 9i). It can be clearly observed that **4**, **5** and **0** all exhibit red emission.

Near-IR luminescence. In the recent several decades, RE-based near-infrared (NIR) luminescence materials have attracted significant interest due to extensive applications in the fields of light emitting diodes, telecommunication and medical science on account of their potential for non-invasive *in vivo* imaging.[59] As a consequence, the NIR luminescence properties of the solid sample of **3** have also been probed at ambient temperature. As demonstrated in Fig. 9j, the NIR emission spectrum under excitation at 581 nm reveals three groups of characteristic bands, corresponding to the $^4F_{3/2} \rightarrow {}^4I_{9/2}$ (876 and 896 nm), $^4F_{3/2} \rightarrow {}^4I_{11/2}$ (1062 nm) and $^4F_{3/2} \rightarrow {}^4I_{13/2}$ (1334 nm) transitions of Nd^{3+} ions.[50c,60] The excitation spectrum of **3** was collected by monitoring the strongest $^4F_{3/2} \rightarrow {}^4I_{11/2}$ emission (Fig. 9k) and exhibits a broad band in the 560 to 610 region, which stems from spin-forbidden Mn^{4+}-crystal-field transitions of $^4A_2 \rightarrow {}^2T_1$ and $^4A_2 \rightarrow {}^2T_2$.[51a] Moreover, its luminescence decay curve was also recorded (Fig. 9l) and fitted by a double exponential function, affording τ_1 and τ_2 of 1.08 μs (25.42%) and 10.44 μs (74.58%) and an average lifetime of 8.07 μs.

Conclusions

To summarize, two types of novel REOCWPOMBMs **1–13** have been successfully prepared by utilizing a step-by-step synthetic strategy in aqueous solution. To the best of our knowledge, they represent the first examples of Waugh-type manganomolybdates functionalized by rare-earth ions and isonicotinic acid ligands. Interestingly, two Waugh-type $[MnMo_9O_{32}]^{6-}$ units are linked through a dinuclear $\{[RE(Hina)(ina)(H_2O)_2]_2\}^{4+}$ cation in **1–3** and the molecular structures of **4–13** comprise an organic–inorganic hybrid $[RE(Hina)_2(H_2O)_6]^{3+}$ fragment and one $[MnMo_9O_{32}]^{6-}$ anion. Experimental results indicate that they exhibit photocatalytic activities for the degradation of azophloxine and the photocatalytic properties of **3** and **8** have been discussed in detail. Interestingly, at pH = 2.6, the catalyst of VT-TiO_2 : **3**/**8** = 1 : 2 behaves with good photocatalytic activity under both UV light and visible light. Moreover, the PL properties and lifetimes of **3–5** have also been investigated. The near-IR emission spectrum of **3** exhibits three characteristic bands that are ascribed to $^4F_{3/2} \rightarrow {}^4I_J$ (J = 9/2, 11/2, 13/2) transitions, the visible emission spectrum of **4** exhibits three characteristic bands attributed to $^4G_{5/2} \rightarrow {}^6H_J$ (J = 5/2, 7/2, 9/2) transitions and a strong band assigned to the $^2E \rightarrow {}^4A_2$ transition of the Mn^{4+} cation in the $[MnMo_9O_{32}]^{6-}$ fragment and **5** exhibits three characteristic emission peaks due to $^5D_0 \rightarrow {}^7F_J$ (J = 0, 1, 2) transitions and a strong band assigned to the $^2E \rightarrow {}^4A_2$ transition of the Mn^{4+} cation in the $[MnMo_9O_{32}]^{6-}$ fragment. This work not only develops an effective synthetic methodology in preparing REOCWPOMBMs and fertilizes the structural multiformity of REOCWPOMBMs and POMB chemistry, but also extends the application aspects of REOCWPOMBMs in the fields of photocatalysis and photoluminescence. These research fruits will drive us to persistently explore and prepare much more novel RECPs with the aim of searching for some reaction rules and intriguing properties. Continuous work and unremitting efforts are under way.

Acknowledgements

This work was supported by the Natural Science Foundation of China (21301049, U1304208, 21571048, 21671054), the Program for Science & Technology Innovation Talents in Universities of Henan Province (16HASTIT001), the Innovation Scientists and Technicians Troop Construction Projects of Henan Province, the Foundation of Education Department of Henan Province (16A150027), the Postdoctoral Foundation of Henan Province (20140025), the Foundation of State Key Laboratory of Structural Chemistry (20160016), the 2014 Special Foundation for Scientific Research Project of Henan University (XXJC20140001), the 2012 Young Backbone Teachers Foundation from Henan Province (2012GGJS-027), the Foundation of Education Department of Henan Province (16A150027) and the Students Innovative Pilot Plan of Henan University (15NA002).

References

1 (*a*) J. T. Rhule, C. L. Hill, D. A. Judd and R. F. Schinazi, *Chem. Rev.*, 1998, **98**, 327; (*b*) J. Lehmann, A. Gaita-Arino, E. Coronado and D. Loss, *Nat. Nanotechnol.*, 2007, **2**, 312; (*c*) D. L. Long, R. Tsunashima and L. Cronin, *Angew. Chem., Int. Ed.*, 2010, **49**, 1736; (*d*) M. T. Pope and A. Müller, *Angew. Chem., Int. Ed. Engl.*, 1991, **30**, 34; (*e*) J. M. Clemente-Juan, E. Coronado and A. Gaita-Arino, *Chem. Soc. Rev.*, 2012, **41**, 7464; (*f*) B. Liu, Z.-T. Yu, J. Yang, W. Hua, Y.-Y. Liu and J.-F. Ma, *Inorg. Chem.*, 2011, **50**, 8967; (*g*) L. Huang, S.-S. Wang, J.-W. Zhao, L. Cheng and G.-Y. Yang, *J. Am. Chem. Soc.*, 2014, **136**, 7637; (*h*) J. Zhou, J.-W. Zhao, Q. Wei, J. Zhang and G.-Y. Yang, *J. Am. Chem. Soc.*, 2014, **136**, 5065.

2 (*a*) M. Lowe, J. Lockhart, G. Forsyth, W. Clegg and K. Fraser, *J. Chem. Soc., Dalton Trans.*, 1995, 145; (*b*) T. Akutagawa, D. Endo, S.-I. Noro, L. Cronin and T. Nakamura, *Coord. Chem. Rev.*, 2007, **251**, 2547; (*c*) A. Dolbecq, E. Dumas, C. R. Mayer and P. Mialane, *Chem. Rev.*, 2010, **110**, 6009.

3 (*a*) U. Kortza, A. Müller, J. V. Slageren, J. Schnack, N. S. Dalal and M. Dressel, *Coord. Chem. Rev.*, 2009, **253**, 2315; (*b*) P. Putaj and F. Lefebvre, *Coord. Chem. Rev.*, 2011, **255**, 1642; (*c*) S. T. Zheng and G. Y. Yang, *Chem. Soc. Rev.*, 2012, **41**, 7623.

4 R. M. Yu, X. F. Kuang, X. Y. Wu, C. Z. Lu and J. P. Donahue, *Coord. Chem. Rev.*, 2009, **253**, 2872.

5 (*a*) C. D. Wu, C. Z. Lu, H. H. Zhuang and J. S. Huang, *J. Am. Chem. Soc.*, 2002, **124**, 3836; (*b*) J. Y. Niu, M. L. Wei, J. P. Wang and D. B. Dang, *Eur. J. Inorg. Chem.*, 2004, **1**, 160; (*c*) H. Y. An, Y. G. Li, D. R. Xiao, E. B. Wang and C. Y. Sun, *Cryst. Growth Des.*, 2006, **6**, 1107; (*d*) X. L. Hao, M. F. Luo, W. Yao, Y. G. Li, Y. H. Wang and E. B. Wang, *Dalton Trans.*, 2011, **40**, 5971; (*e*) X. J. Feng, H. Y. Han, Y. H. Wang, L. L. Li, Y. G. Li and E. B. Wang, *CrystEngComm*, 2013, **15**, 7267.

6 (*a*) H. H. Zhao, M. J. Bazile, J. R. Galán-Mascarós and K. R. Dunbar, *Angew. Chem., Int. Ed.*, 2003, **42**, 1015; (*b*) N. Ishikawa, S. Otsuka and Y. Kaizu, *Angew. Chem., Int. Ed.*, 2005, **44**, 731; (*c*) V. Tsaryuk, K. Zhuravlev, V. Zolin, P. Gawryszewska, P. Legendziewicz, V. Kudryashova and I. Pekareva, *J. Photochem. Photobiol., A*, 2006, **177**, 314; (*d*) M. D. Allendorf, C. A. Bauer, R. K. Bhakta and R. J. T. Houk, *Chem. Soc. Rev.*, 2009, **38**, 1330; (*e*) X. J. Kong, Y. L. Wu, L. S. Long, L. S. Zheng and Z. P. Zheng, *J. Am. Chem. Soc.*, 2009, **131**, 6918; (*f*) P. Y. Wu, J. Wang, Y. M. Li, C. He, Z. Xie and C. Y. Duan, *Adv. Funct. Mater.*, 2011, **21**, 2788; (*g*) B. F. Wicker, H. Fan, A. K. Hickey, M. G. Crestani, J. Scott, M. Pink and D. J. Mindiola, *J. Am. Chem. Soc.*, 2012, **134**, 20081.

7 (*a*) N. Dupré, P. Rémy, K. Micoine, C. Boglio, S. Thorimbert, E. Lacôte, B. Hasenknopf and M. Malacria, *Chem. – Eur. J.*, 2010, **16**, 7256; (*b*) C. Boglio, G. Lemière, B. Hasenknopf, S. Thorimbert, E. Lacote and M. Malacria, *Angew. Chem., Int. Ed.*, 2006, **45**, 3324; (*c*) Y. Kikukawa, S. Yamaguchi, Y. Nakagawa, K. Uehara, S. Uchida, K. Yamaguchi and N. Mizuno, *J. Am. Chem. Soc.*, 2008, **130**, 15872; (*d*) P. Mialane, A. Dolbecq and F. Sécheresse, *Chem. Commun.*, 2006, 3477; (*e*) X. Ma, W. Yang, L. J. Chen and J. W. Zhao, *CrystEngComm*, 2015, **17**, 8175.

8 R. D. Peacock and T. J. R. Weakley, *J. Chem. Soc. A*, 1971, 1836.

9 (*a*) B. S. Bassil, M. H. Dickman, B. von der Kammer and U. Kortz, *Inorg. Chem.*, 2007, **46**, 2452; (*b*) X. Y. Liu, Y. Y. Jia, Y. F. Zhang and R. D. Huang, *Eur. J. Inorg. Chem.*, 2010, **25**, 4027; (*c*) K. Suzuki, M. Sugawa, Y. Kikukawa, K. Kamata, K. Yamaguchi and N. Mizuno, *Inorg. Chem.*, 2012, **51**, 6953.

10 (*a*) M. Sadakane, M. H. Dickman and M. T. Pope, *Inorg. Chem.*, 2001, **40**, 2715; (*b*) X. F. Fang, T. M. Anderson, C. Benell and C. L. Hill, *Chem. – Eur. J.*, 2005, **11**, 712; (*c*) W. L. Huang, M. Schopfer, C. Zhang, R. C. Howell, L. Todaro, B. A. Gee, L. C. Francesconi and T. Polenova, *J. Am. Chem. Soc.*, 2008, **130**, 481; (*d*) J. Y. Niu, K. H. Wang, H. N. Chen, J. W. Zhao, P. T. Ma, J. P. Wang, M. X. Li, Y. Bai and D. B. Dang, *Cryst. Growth Des.*, 2009, **9**, 4362; (*e*) S. W. Zhang, Y. Wang, J. W. Zhao, P. T. Ma, J. P. Wang and J. Y. Niu, *Dalton Trans.*, 2012, **41**, 3764.

11 (*a*) K. Wassermann, M. H. Dickman and M. T. Pope, *Angew. Chem., Int. Ed. Engl.*, 1997, **36**, 1445; (*b*) K. Fukaya and T. Yamase, *Angew. Chem., Int. Ed.*, 2003, **42**, 654; (*c*) F. Hussain, F. Conrad and G. R. Patzke, *Angew. Chem., Int. Ed.*, 2009, **48**, 9088; (*d*) C. Ritchie, E. G. Moore, M. Speldrich, P. Kögerler and C. Boskovic, *Angew. Chem., Int. Ed.*, 2010, **49**, 7702; (*e*) C. Ritchie, M. Speldrich, R. W. Gable, L. Sorace, P. Kögerler and C. Boskovic, *Inorg. Chem.*, 2011, **50**, 7004; (*f*) Y. Wang, X. P. Sun, S. Z. Li, P. T. Ma, J. P. Wang and J. Y. Niu, *Dalton Trans.*, 2015, **44**, 733.

12 (*a*) J. P. Wang, X. Y. Duan, X. D. Du and J. Y. Niu, *Cryst. Growth Des.*, 2006, **6**, 2266; (*b*) B. S. Bassil, M. H. Dickman, I. Römer, B. von der Kammer and U. Kortz, *Angew. Chem., Int. Ed.*, 2007, **46**, 6192; (*c*) S. Reinoso, M. Giménea-Marqués, J. Galán-Mascarós, P. Vitoria and J. M. Gutiérrez-Zorrilla, *Angew. Chem., Int. Ed.*, 2010, **49**, 8384.

13 (*a*) A. H. Ismail, B. S. Bassil, A. Suchoparand and U. Kortz, *Eur. J. Inorg. Chem.*, 2009, **34**, 5247; (*b*) A. H. Ismail, M. H. Dickman and U. Kortz, *Inorg. Chem.*, 2009, **48**, 1559; (*c*) D. D. Liu, Y. G. Chen, C. J. Zhang, H. X. Meng, Z. C. Zhang and C. X. Zhang, *J. Solid State Chem.*, 2011, **184**, 1355; (*d*) W. C. Chen, X. L. Wang, Y. Q. Jiao, P. Huang, E. L. Zhou, Z. M. Su and K. Z. Shao, *Inorg. Chem.*, 2014, **53**, 9486; (*e*) L. Y. Song, D. D. Zhang, P. T. Ma, Z. J. Liang, J. P. Wang and J. Y. Niu, *CrystEngComm*, 2013, **15**, 4597.

14 (*a*) H. Y. An, Z. B. Han and T. Q. Xu, *Inorg. Chem.*, 2010, **49**, 11403; (*b*) M. Ibrahim, S. S. Mal, B. S. Bassil, A. Banerjee and U. Kortz, *Inorg. Chem.*, 2011, **50**, 956; (*c*) K. Y. Cui, F. Y. Li, L. Xu, B. B. Xu, N. Jiang, Y. C. Wang and J. P. Zhang, *Dalton Trans.*, 2012, **41**, 4871; (*d*) W. C. Chen, H. L. Li, X. L. Wang, K. Z. Shao, Z. M. Su and E. B. Wang, *Chem. – Eur. J.*, 2013, **19**, 11007; (*e*) A. H. Ismail, B. S. Bassil, I. Römer and U. Kortz, *Z. Anorg. Allg. Chem.*, 2013, **639**, 2510.

15 (*a*) J. W. Zhao, H. L. Li, Y. Z. Li, C. Y. Li, Z. L. Wang and L. J. Chen, *Cryst. Growth Des.*, 2014, **14**, 5495; (*b*) H. L. Li, W. Yang, Y. Chai, L. J. Chen and J. W. Zhao, *Inorg. Chem. Commun.*, 2015, **56**, 35; (*c*) W. Yang, H. L. Li, Y. Y. Li, L. J. Chen and J. W. Zhao, *Inorg. Chem. Commun.*, 2015, **60**, 71.

16 J. W. Zhao, J. L. Zhang, Y. Z. Li, J. Cao and L. J. Chen, *Cryst. Growth Des.*, 2014, **14**, 1467.

17 V. Shivaiah, P. V. N. Reddy, L. Cronin and S. K. Das, *J. Chem. Soc., Dalton Trans.*, 2002, 3781.

18 (*a*) D. Drewes and B. Krebs, *Z. Anorg. Allg. Chem.*, 2005, **631**, 2591; (*b*) H. Y. An, D. R. Xiao, E. B. Wang, Y. G. Li, X. L. Wang and L. Xu, *Eur. J. Inorg. Chem.*, 2005, **2005**, 854.

19 H. Zhang, L. Y. Duan, Y. Lan, E. B. Wang and C. W. Hu, *Inorg. Chem.*, 2003, **42**, 8053.

20 J. Y. Niu, M. L. Wei, J. P. Wang and D. B. Dang, *Eur. J. Inorg. Chem.*, 2004, 160.

21 X. Y. Chen, Y. P. Chen, Z. M. Xia, H. B. Hu, Y. Q. Sun and W. Y. Huang, *Dalton Trans.*, 2012, **41**, 10035.

22 H. Struve, *J. Prakt. Chem.*, 1854, **61**, 499.

23 (*a*) L. O. Gavrilova and V. N. Molchanov, *Russ. J. Coord. Chem.*, 2005, **31**, 401; (*b*) H. Q. Tan and E. B. Wang, *Zhongguo Keji Lunwen Zaixian*, 2010, **5**, 233.

24 (*a*) G. M. Sheldrick, *SHELXS 97, Program for Crystal Structure Solution*, University of Göttingen, Göttingen, Germany, 1997; (*b*) G. M. Sheldrick, *SHELXL 97, Program for Crystal Structure Refinement*, University of Göttingen, Germany, 1997.

25 (*a*) M. Sadakane and E. Steckhan, *Chem. Rev.*, 1998, **98**, 219; (*b*) T. Okuhara, N. Mizuno and M. Misono, *Adv. Catal.*, 1996, **41**, 113; (*c*) T. Takashima, R. Nakamura and K. Hashimoto, *J. Phys. Chem. C*, 2009, **113**, 17247; (*d*) T. Yamase, X. O. Cao and S. Yazaki, *J. Mol. Catal. A: Chem.*, 2007, **262**, 119; (*e*) R. Cao, T. M. Anderson, D. A. Hillesheim, P. Kögerler, K. I. Hardcastle and C. L. Hill, *Angew. Chem., Int. Ed.*, 2008, **47**, 9380; (*f*) Y. V. Geletii, Z. Huang, Y. Hou, D. G. Musaev, T. Lian and C. L. Hill, *J. Am. Chem. Soc.*, 2009, **131**, 7522; (*g*) A. E. Kuznetsov, Y. V. Geletii, C. L. Hill, K. Morokuma and D. G. Musaev, *J. Am. Chem. Soc.*, 2009, **131**, 6844; (*h*) K. Binnemans, *Chem. Rev.*, 2009, **109**, 4283; (*i*) D.-Y. Shi, J.-W. Zhao, L.-J. Chen, P.-T. Ma, J.-P. Wang and J.-Y. Niu, *CrystEngComm*, 2012, **14**, 3108; (*j*) H. L. Li, Y. J. Liu, R. Zheng, L. J. Chen, J.-W. Zhao and G.-Y. Yang, *Inorg. Chem.*, 2016, **55**, 3881.

26 (*a*) H. L. Li, W. Yang, X. H. Wang, L. J. Chen, J. R. Ma, L. W. Zheng and J. W. Zhao, *Cryst. Growth Des.*, 2016, **16**, 108; (*b*) J. W. Zhao, D. Y. Shi, L. J. Chen, Y. Z. Li, P. T. Ma, J. P. Wang and J. Y. Niu, *Dalton Trans.*, 2012, **41**, 10740; (*c*) J. W. Zhao, H. L. Li, Y. Z. Li, C. Y. Li, Z. L. Wang and L. J. Chen, *Cryst. Growth Des.*, 2014, **14**, 5495.

27 (*a*) R. C. Howell, F. G. Perez, S. Jain, W. D. Horrocks, A. L. Rheingold and L. C. Francesconi, *Angew. Chem., Int. Ed.*, 2001, **40**, 4031; (*b*) X. L. Wang, Y. Q. Guo, Y. G. Li, E. B. Wang, C. W. Hu and N. H. Hu, *Inorg. Chem.*, 2003, **42**, 4135.

28 (*a*) H. Q. Tan, Y. G. Li, Z. M. Zhang, C. Qin, X. L. Wang, E. B. Wang and Z. M. Su, *J. Am. Chem. Soc.*, 2007, **129**, 10066; (*b*) H. Q. Tan, Y. G. Li, W. L. Chen, D. Liu, Z. M. Su, Y. Lu and E. B. Wang, *Chem. – Eur. J.*, 2009, **15**, 10940.

29 (*a*) S. B. Yu and A. B. Watson, *Chem. Rev.*, 1999, **99**, 2353; (*b*) S. M. Malinak, K. D. Demadis and D. Coucouvanis, *J. Am. Chem. Soc.*, 1995, **117**, 3126; (*c*) Z. S. Meng, F. S. Guo, J. L. Liu, J. D. Leng and M. L. Tong, *Dalton Trans.*, 2012, **41**, 2320; (*d*) Z. R. Pan, J. Xu, H. G. Zheng, K. X. Huang, Y. Z. Li, Z. J. Guo and S. R. Batten, *Inorg. Chem.*, 2009, **48**, 5772; (*e*) X. Zhao, F. Zhou, Q. Liu, Q. F. Chen, J. Y. Yang, W. H. Zhang, Y. L. Song and J. P. Lang, *Inorg. Chem.*, 2016, **55**, 1861.

30 (*a*) M. Feliz, J. M. Garriga, R. Llusar, S. Uriel, M. G. Humphrey, N. T. Lucas, M. Samoc and B. Luther-Davies, *Inorg. Chem.*, 2001, **40**, 6132; (*b*) M. Feliz, E. Guillamón, R. Llusar, C. Vicent, S. E. Stiriba, J. P. Prieto and M. Barberis, *Chem. – Eur. J.*, 2006, **12**, 1486; (*c*) R. Llusar and S. Uriel, *Eur. J. Inorg. Chem.*, 2003, 1271.

31 Z. Pan, J. Xu, H. Zheng, K. Huang, Y. Li, Z. Guo and S. R. Batten, *Inorg. Chem.*, 2009, **48**, 5772.

32 (*a*) U. Kortz, A. Tézé and G. Hervé, *Inorg. Chem.*, 1999, **38**, 2038; (*b*) J. M. Clemente-Juan, E. Coronado, J. R. Galán-Mascarós and C. J. Gómez-García, *Inorg. Chem.*, 1999, **38**, 55; (*c*) B. Nohra, P. Mialane, A. Dolbecq, E. Rivière, J. Marrot and F. Sécheresse, *Chem. Commun.*, 2009, 2703; (*d*) X. Fang, M. Speldrich, H. Schilder, R. Cao, K. P. O'Halloran, C. L. Hill and P. Kögerler, *Chem. Commun.*, 2010, **46**, 2760; (*e*) J.-W. Zhao, H.-P. Jia, J. Zhang, S.-T. Zheng and G.-Y. Yang, *Chem. – Eur. J.*, 2007, **13**, 10030; (*f*) H.-M. Zhang, Y.-G. Li, Y. Lu, R. Clérac, Z.-M. Zhang, Q. Wu, X.-J. Feng and E.-B. Wang, *Inorg. Chem.*, 2009, **48**, 10889; (*g*) Q. Wu, Y.-G. Li, Y.-H. Wang, E.-B. Wang, Z.-M. Zhang and R. Clérac, *Inorg. Chem.*, 2009, **48**, 1606; (*h*) X.-B. Han, Z.-M. Zhang, T. Zhang, Y.-G. Li, W. Lin, W. You, Z.-M. Su and E.-B. Wang, *J. Am. Chem. Soc.*, 2014, **136**, 5359.

33 (*a*) I. D. Brown and D. Altermatt, *Acta Crystallogr., Sect. B: Struct. Sci.*, 1985, **41**, 244; (*b*) H. H. Thorp, *Inorg. Chem.*, 1992, **31**, 1585.

34 (*a*) P. Mialane, A. Dolbecq, E. Rivière, J. Marrot and F. Sécheresse, *Eur. J. Inorg. Chem.*, 2004, 33; (*b*) M. K. Saini, R. Gupta, S. Parbhakar, A. K. Mishra, R. Mathur and F. Hussain, *RSC Adv.*, 2014, **4**, 25357; (*c*) U. Kortz, *J. Cluster Sci.*, 2003, **14**, 205.

35 C.-G. Yuan, Y.-X. Zhang, Y. Gao, D.-Q. Zhang, L.-L. Yang and H.-W. Yan, *Hebei Daxue Xuebao, Ziran Kexueban*, 2002, **22**, 19.

36 (*a*) W. M. Wesley and W. G. H. Harry, *Reflectance Spectroscopy*, Wiley, New York, 1966; (*b*) J. I. Pankove, *Optical Processes in Semiconductors*, Prentice-Hall, Englewood Cliffs, NJ, 1997; (*c*) Y. Xia, P. Wu, Y. Wei, Y. Wang and H. Guo, *Cryst. Growth Des.*, 2006, **6**, 253.

37 (*a*) E. Selli, *Phys. Chem. Chem. Phys.*, 2002, **4**, 6123; (*b*) H. Zollinger, *Color Chemistry – Synthesis*, Properties and Application of Organic Dyes and Pigments, VCH, New York, 1987.

38 (*a*) H. Zhang, D. Chen, X. J. Lv, Y. Wang, H. X. Chang and J. H. Li, *Environ. Sci. Technol.*, 2010, **44**, 1107; (*b*) J. M. Joseph, H. Destaillats, H.-M. Hung and M. R. Hoffmann, *J. Phys. Chem. A*, 2000, **104**, 301; (*c*) A. Dolbecq, P. Mialane, B. Keita and L. Nadjo, *J. Mater. Chem.*, 2012, **22**, 24509; (*d*) N. Chahbane, D.-L. Popescu, D. A. Mitchell, A. Chanda, D. Lenoir, A. D. Ryabov, K.-W. Schramm and T. J. Collins, *Green Chem.*, 2007, **9**, 49; (*e*) X. Cai, B. Han, S. Deng, Y. Wang, C. Dong, Y. Wang and I. Djerdj, *CrystEngComm*, 2014, **16**, 7761.

39 (*a*) B. Liu, Z. T. Yu, J. Yang, W. Hua, Y. Y. Liu and J. F. Ma, *Inorg. Chem.*, 2011, **50**, 8967; (*b*) Y. Q. Chen, G. R. Li, Y. K. Qu, Y. H. Zhang, K. H. He, Q. Gao and X. H. Bu, *Cryst. Growth Des.*, 2013, **13**, 901; (*c*) B. L. Fei, W. Li, J. H. Wang, Q. B. Liu, J. Y. Long, Y. G. Li, K. Z. Shao, Z. M. Su and W. Y. Sun, *Dalton Trans.*, 2014, **43**, 10005; (*d*) H. M. Zhang, J. Yang, W. Q. Kan, Y. Y. Liu and J. F. Ma, *Cryst. Growth Des.*, 2016, **16**, 265.

40 (*a*) Priyanka and V. C. Srivastava, *Ind. Eng. Chem. Res.*, 2013, **52**, 17790; (*b*) T. S. Jamil, M. Y. Ghaly, N. A. Fathy, A. E. T. A. Halim and L. Osterlund, *Sep. Purif. Technol.*, 2012, **98**, 270.

41 (*a*) K. Vinodgopal, D. E. Wynkoop and P. V. Kamat, *Environ. Sci. Technol.*, 1996, **30**, 1660; (*b*) C. Bauer, P. Jacques and A. Kalt, *J. Photochem. Photobiol., A*, 2001, **140**, 87; (*c*) A. Troupis, T. M. Triantis, E. Gkika, A. Hiskia and E. Papaconstantinou, *Appl. Catal., B*, 2009, **86**, 98.

42 (*a*) M. A. Gondal, X. F. Chang and Z. H. Yamani, *Chem. Eng. J.*, 2010, **165**, 250; (*b*) X. Xiao, R. Hao, M. Liang, X. X. Zuo, J. M. Nan, L. S. Li and W. D. Zhang, *J. Hazard. Mater.*, 2012, **233–234**, 122.

43 (*a*) A. L. Linsebigler, G. Lu and J. T. Yates, *Chem. Rev.*, 1995, **95**, 735; (*b*) M. R. Hoffmann, S. T. Martin, W. Y. Choi and D. W. Bahnemann, *Chem. Rev.*, 1995, **95**, 69; (*c*) A. Fujishima, T. N. Rao and D. A. Tryk, *J. Photochem. Photobiol., C*, 2000, **1**, 1; (*d*) D. Chatterjee and S. Dasgupta, *J. Photochem. Photobiol., C*, 2005, **6**, 186; (*e*) X. Chen and S. S. Mao, *Chem. Rev.*, 2007, **107**, 2891; (*f*) A. Fujishima, X. Zhang and D. A. Tryk, *Surf. Sci. Rep.*, 2008, **63**, 515.

44 (*a*) A. Hiskia, A. Mylonas and E. Papaconstantinou, *Chem. Soc. Rev.*, 2001, **30**, 62; (*b*) Y. Guo and C. Hu, *J. Mol. Catal. A: Chem.*, 2007, **262**, 136; (*c*) H. Yang, T. Liu, M. Cao, H. Li, S. Gao and R. Cao, *Chem. Commun.*, 2010, **46**, 2429; (*d*) R. N. Biboum, C. P. Nanseu Njiki, G. Zhang, U. Kortz, P. Mialane, A. Dolbecq, I. M. Mbomekalle, L. Nadjo and B. Keita, *J. Mater. Chem.*, 2011, **21**, 645; (*e*) S. Kim, J. Yeo and W. Choi, *Appl. Catal., B*, 2008, **84**, 148; (*f*) J. Huang, C. Tao, Q. An, W. Zhang, Y. Wu, X. Li, D. Shen and G. Li, *Chem. Commun.*, 2010, **46**, 967.

45 (*a*) N. Lu, Y. H. Zhao, H. B. Liu, Y. H. Guo, X. Yuan, H. Xu, H. F. Peng and H. W. Qin, *J. Hazard. Mater.*, 2012, **199–200**, 1; (*b*) S. K. Kansal, M. Singh and D. Sud, *J. Hazard. Mater.*, 2007, **141**, 581.

46 (*a*) Y. Yang, Y. H. Guo, C. W. Hu, C. J. Jiang and E. B. Wang, *J. Mater. Chem.*, 2003, **13**, 1686; (*b*) L. Xu, X. Yang, Y. H. Guo, F. Y. Ma, Y. N. Guo, X. Yuan and M. X. Huo, *J. Hazard. Mater.*, 2010, **178**, 1070.

47 (*a*) J. Rocha, L. D. Carlos, F. A. A. Paz and D. Ananias, *Chem. Soc. Rev.*, 2011, **40**, 926; (*b*) L. D. Carlos, R. A. S. Ferreira, V. de Z. Bermudez and S. J. L. Ribeiro, *Adv. Mater.*, 2009, **21**, 509; (*c*) Y. J. Cui, Y. F. Yue, G. D. Qian and B. L. Chen, *Chem. Rev.*, 2012, **112**, 1126; (*d*) X. D. Wang, O. S. Wolfbeis and R. J. Meier, *Chem. Soc. Rev.*, 2013, **42**, 7834; (*e*) L. Armelao, S. Quici, F. Barigelletti, G. Accorsi, G. Bottaro, M. Cavazzini and E. Tondello, *Coord. Chem. Rev.*, 2010, **254**, 487.

48 (*a*) J.-C. G. Bünzli, *Chem. Rev.*, 2010, **110**, 2729; (*b*) H. L. Li, Y. J. Liu, R. Zheng, L. J. Chen, J. W. Zhao and G. Y. Yang, *Inorg. Chem.*, 2016, **55**, 3881; (*c*) Y. Li, F. K. Zheng, X. Liu, W. Q. Zou, C. Guo, C. Z. Lu and J. S. Huang, *Inorg. Chem.*, 2006, **45**, 6308.

49 (*a*) T. Yamase, *Chem. Rev.*, 1998, **98**, 307; (*b*) T. Yamase, T. Kobayashi, M. Sugeta and H. Naruke, *J. Phys. Chem. A*, 1997, **101**, 5046; (*c*) T. Ozeki and T. Yamase, *J. Alloys Compd.*, 1993, **192**, 28; (*d*) C. Ritchie, E. G. Moore, M. Speldrich, P. Kgerler and C. Boskovic, *Angew. Chem., Int. Ed.*, 2010, **49**, 7702; (*e*) C. Ritchie, V. Baslon, E. G. Moore, C. Reber and C. Boskovic, *Inorg. Chem.*, 2012, **51**, 1142; (*f*) J. W. Zhao, J. Cao, Y. Z. Li, J. Zhang and L. J. Chen, *Cryst. Growth Des.*, 2014, **14**, 6217.

50 (*a*) H. Yang, C. L. Hu and J. G. Mao, *Inorg. Chem.*, 2016, **55**, 6051; (*b*) H. L. Li, W. Yang, X. H. Wang, L. J. Chen, J. R. Ma, L. W. Zheng and J. W. Zhao, *Cryst. Growth Des.*, 2016, **16**, 108; (*c*) L. L. Li, G. J. Cao, J. W. Zhao, H. He, B. F. Yang and G. Y. Yang, *Inorg. Chem.*, 2016, **55**, 5671.

51 (*a*) T. Yamase, T. Kobayashi and S. F. A. Keith, *J. Electrochem. Soc.*, 1996, **143**, 1678; (*b*) Y. D. Xu, D. Wang, L. Wang, N. Ding, M. Shi, J. G. Zhong and S. Qi, *J. Alloys Compd.*, 2013, **550**, 226.

52 (*a*) Z. Ahmed, W. A. Dar and K. Iftikhar, *Inorg. Chim. Acta*, 2012, **392**, 446; (*b*) H. F. Brito, O. L. Malta, M. C. F. C. Felinto, E. E. S. Teotonio, J. F. S. Menezes, C. F. B. Silva, C. S. Tomiyama and C. A. A. Carvalho, *J. Alloys Compd.*, 2002, **344**, 293; (*c*) R. Ilmi and K. Iftikhar, *Inorg. Chem. Commun.*, 2010, **13**, 1552.

53 (*a*) P. L. Li, Z. J. Wang, Z. P. Yang and Q. L. Guo, *Opt. Commun.*, 2014, **332**, 83; (*b*) J. Zhou and Z. G. Xia, *J. Mater. Chem. C*, 2015, **3**, 7552.

54 P. Mialane, L. Lisnard, A. Mallard, J. Marrot, E. Antic-Fidancev, P. Aschehoug, D. Vivien and F. Sécheresse, *Inorg. Chem.*, 2003, **42**, 2102.

55 Y. J. Cui, Y. F. Yue, G. D. Qian and B. L. Chen, *Chem. Rev.*, 2012, **112**, 1126.

56 (*a*) Y. Hasegawa, M. Yamamuro, Y. Wada, N. Kanehisa, Y. Kai and S. J. Yanagida, *J. Phys. Chem. A*, 2003, **107**, 1697; (*b*) Y. Hasegawa, M. Iwamuro, K. Murakoshi, Y. Wada, R. Arakawa, T. Yamanaka, N. Nakashima and S. J. Yanagida, *Bull. Chem. Soc. Jpn.*, 1998, **71**, 2573; (*c*) Y. Hasegawa, Y. Wada and S. J. Yanagida, *J. Photochem. Photobiol., C*, 2004, **5**, 183.

57 (*a*) A. F. Kirby and F. S. Richardson, *J. Phys. Chem.*, 1983, **87**, 2544; (*b*) J. W. Stouwdam and F. C. J. M. van Veggel, *Nano Lett.*, 2002, **2**, 733; (*c*) Y. G. Su, L. P. Li and G. S. Li, *Chem. Mater.*, 2008, **20**, 6060.

58 Y. Zhang, W. T. Gong, J. J. Yu, H. C. Pang, Q. Song and G. L. Ning, *RSC Adv.*, 2015, **5**, 62527.

59 J.-C. G. Bünzli and C. Piguet, *Chem. Soc. Rev.*, 2005, **34**, 1048.

60 (*a*) R. M. Abdelhameed, L. D. Carlos, A. M. S. Silva and J. Rocha, *Chem. Commun.*, 2013, **49**, 5019; (*b*) F. Eckes, V. Bulach, A. Guenet, C. A. Strassert, L. Cola and M. Hosseini, *Chem. Commun.*, 2010, **46**, 619.

